Article │ Received 31 December 2024; Accepted 27 March 2025; Published 18 April 2025
https://doi.org/10.55092/sc20250007

Numerical investigation of seismic performance and size effect in CFRP-reinforced concrete shear walls

Bo Li[1], Dong Li[1], Fengjuan Chen[1,2,3]*, Liu Jin[1] and Xiuli Du[1]

[1] The Key Laboratory of Urban Security and Disaster Engineering, Beijing University of Technology, Beijing 100124, China
[2] Chongqing Research Institute of Beijing University of Technology, Chongqing 400030, China
[3] Nuclear Industry X Intelligence Laboratory, Beijing University of Technology, Beijing 100124, China

* Correspondence author; E-mail: fengjuanchen@bjut.edu.cn.

Highlights:

- CFRP-RC composites boost seismic resilience via strength-to-weight ratio and self-centering.
- Size-effect mechanisms under combined geometric/reinforcement parameters remain underexplored.
- Advances performance-based design of corrosion-resistant, low-residual-deformation structures.
- Refined size-effect model integrates CFRP strain for improved damage prediction.

Abstract: Addressing conventional reinforced concrete (RC) shear walls' susceptibility to brittle failure and residual deformation during earthquakes; this study investigates carbon fiber reinforced polymer (CFRP)-RC composites for enhanced seismic resilience. CFRP's superior strength-to-weight ratio; corrosion resistance; and self-centering potential address post-earthquake reparability challenges. Current knowledge gaps persist in size-effect mechanisms under combined geometric and reinforcement parameters (shear span ratio; horizontal reinforcement ratio; height-to-thickness ratio). Numerical analysis of 28 models evaluates hysteretic behavior; strength degradation patterns; ductility coefficients; and residual deformation characteristics. A refined size-effect model incorporating CFRP's strain distribution overcomes existing predictive limitations; advancing performance-based design of damage-tolerant structures.

Keywords: seismic resilience; self-centering potential; height-to-thickness ratio; residual deformation; size effect

1. Introduction

Reinforced concrete (RC) shear walls constitute a prevalent lateral force-resisting system in earthquake-prone regions due to their validated seismic performance [1–3]. Their failure modes under seismic action primarily divide into bending failure and shear failure, each governed by distinct

influencing factors [4–5]. While modern design theories have matured to ensure stable energy dissipation capacity, persistent challenges in post-earthquake repair, corrosion resistance, and residual deformation control hinder their long-term reliability [6–9].

Recent advancements in shear wall retrofitting have demonstrated the efficacy of material substitution strategies for seismic enhancement. Yang *et al.* [10] optimized the positioning of concrete replacement, revealing that placing C45 concrete at the ends of walls increases bearing capacity while improving energy dissipation and ductility compared to conventional designs. Parallel innovations by Sharma *et al.* [11] employed ultra-high-performance concrete (UHPC) in boundary elements, achieving damage reduction at critical swing angles through enhanced confinement effects. Complementing these findings, Zhang *et al.* [12] systematically quantified seismic improvements in high aspect-ratio walls, where strength upgrades elevated key performance indices, particularly in stiffness retention and hysteresis loop stability. These collective efforts underscore the importance of localized material engineering in seismic retrofitting paradigms.

In engineering practice, the seismic performance of concrete shear walls is influenced by intricate interactions among components, with conflicting effects that complicate soundness assessments [13–14]. Furthermore, the elastoplastic behavior of steel reinforcement leads to large post-earthquake deformations, highlighting the need for self-recovery mechanisms to restore post-seismic functionality [9]. In addition to these challenges, the deterioration of reinforced concrete structures due to steel bar corrosion presents another urgent concern [15–17]. This corrosion not only weakens the overall bearing capacity of the structure but also causes cracking and peeling of the concrete protective layer, ultimately threatening the safety and durability of the building.

Fiber reinforced polymer (FRP) is a type of composite material with high strength, good corrosion resistance, and good fatigue resistance [18–21], and has become a promising alternative to steel bars. After analyzing the mechanical properties of FRP bars and previous studies [22–25], it was found that it is because of the linear elastic properties and low elastic modulus of FRP bars that FRP bars are expected to have advantages in controlling the residual deformation of seismic structures. Ghazi Zadeh *et al.* [26] observed that the GFRP-steel hybrid system has better self-centering performance while maintaining significant energy dissipation capacity, which helps to avoid excessive residual displacement. Mohamed *et al.* [27] conducted a destructive test on four large-scale shear walls under quasi-static repeated horizontal loads and found that GFRP-reinforced shear walls have good strength and deformation capacity and reasonable energy dissipation capacity. In comparison, CFRP bars have better tensile strength and stiffness and show good self-recovery performance in structures. However, there are not many studies on CFRP-reinforced shear walls. Zhao *et al.* [28] conducted a pseudo-static cyclic load test on three full-scale shear walls with the same geometric dimensions. The test results showed that compared with reinforced concrete shear walls, the lateral bearing capacity, post-yield stiffness and energy dissipation capacity of CFRP-reinforced shear walls reached a comparable level.

However, existing experimental paradigms suffer critical limitations: (1) Narrow parameter spaces; (2) Incomplete damage quantification; (3) Absence of multi-hazard durability data. Bridging this knowledge gap requires multi-scale numerical modeling to systematically assess CFRP shear walls under varied seismic spectra, while addressing three key implementation barriers: First, life-cycle economics—the 3–5 times initial cost premium of CFRP [29] necessitates hybrid reinforcement optimization. Second, constructability challenges-ACI 440.5–22 [30] documents a 25–40% increase in installation cycles due to CFRP's

handling sensitivity. Third, durability uncertainties-anchorage systems exhibit strength degradation under hygro-thermal cycling.

Existing studies have demonstrated size effects in conventional reinforced concrete components such as beams [31], plates [32], columns [33], and walls [34]. While current design codes (e.g., CSA A23.3:19, BS EN1992–1–1–2014, ACI 318–2019) partially address size effects in shear design, these provisions remain inadequate for CFRP-reinforced concrete shear walls due to two critical knowledge gaps: (1) the fundamental understanding of CFRP composite behavior in shear walls under seismic loads is still nascent, and (2) existing code formulations lack explicit consideration of size-dependent performance degradation mechanisms specific to CFRP-reinforced systems. Traditional experimental approaches face inherent limitations—key seismic performance parameters (secant stiffness, ductility coefficient) exhibit scale dependency, making it impossible to establish size-independent test benchmarks. This methodological constraint necessitates advanced numerical simulations to systematically investigate both the seismic behavior and intrinsic size effects of CFRP-reinforced shear walls.

To address these dual challenges, this study examines 28 geometrically scaled CFRP-reinforced shear walls through parametric analysis of reinforcement ratio, shear span ratio, height-to-thickness ratio, and structural dimensions. The investigation specifically targets the underexplored coupling between CFRP material characteristics and size effects, quantifying seven critical seismic indicators: ductility coefficient, softening rate, secant stiffness, strength degradation coefficient, maximum displacement ratio, cumulative dissipated energy, and hysteresis loop residual deformation. The derived size effect laws reveal non-negligible scaling distortions in current design assumptions. These findings provide urgently needed theoretical support for developing size-effect-aware design provisions for CFRP shear walls, bridging a critical gap in modern seismic codes.

2. Mesoscopic modelling of CFRP-reinforced concrete shear walls

FEM analysis provides an efficient tool for the parametric analysis and allows a good understanding of the mechanical behavior and the corresponding mechanism of concrete components undergoing the external applied loads, especially for large-scaled concrete shear walls.

2.1. Establishment of CFRP-reinforced shear wall specimen

While the homogenized macro-model effectively simulates structural-level responses [35–38], it inherently neglects mesoscale interactions between concrete constituents. To solve this key scientific problem, this study adopts a multi-scale verification strategy of “macroscopic first, then mesoscopic”: first, the macroscopic model is used to verify the accuracy of the modeling method, and then a mesoscopic model is developed on this basis to reveal the damage mechanism at the material level.

The three-dimensional macroscopic finite element model of CFRP-reinforced shear walls, shown in Figure 1(a), is initially established based on the fundamental principles of structural mechanics and material behavior. In this model, the concrete is represented using solid elements, the CFRP reinforcement is modeled with line elements [37], and the bond-slip effect between them is simulated using connector elements. A fixed constraint is applied at the bottom of the shear wall to restrict movement and ensure structural stability. Meanwhile, the loading beam is placed on top of the wall, and a reference point is set at the same height as each specimen to serve as the horizontal loading point. This

reference point is coupled with the loading beam to constrain all degrees of freedom at the bottom of the foundation and restrict the out-of-plane displacement of the horizontal loading point [38]. Additionally, an axial load is applied above the loading beam to simulate the real stress conditions of the shear wall. Displacement-controlled cyclic loads are then applied at the horizontal loading points to simulate seismic effects, allowing for the analysis of the hysteresis performance and failure mechanism of shear walls under cyclic loading.

This model is rigorously validated by comparing its results with experimental data from previous studies [39], ensuring accuracy and reliability. The specific parameters are shown in Table 1. As illustrated in Figures 1(b) and 1(c), the numerical predictions of shear capacity and failure modes strongly align with experimental test results. This close correlation between simulation and actual test outcomes demonstrates the model's effectiveness in accurately capturing the global seismic behavior of CFRP-reinforced shear walls under different loading conditions.

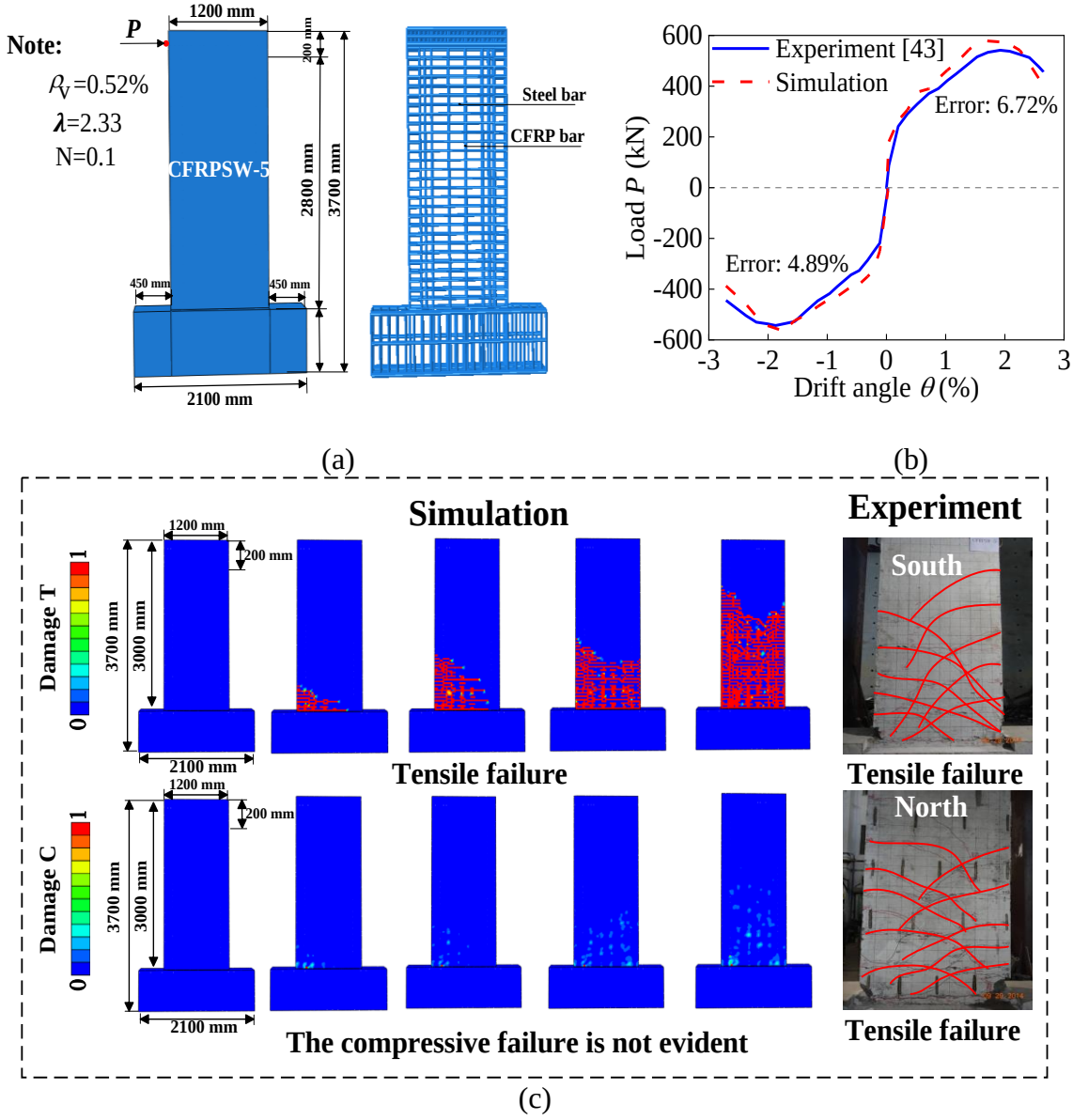

Figure 1. Macro model of CFRP-reinforced shear wall: **(a)** numerical model; **(b)** skeleton curve verification; **(c)** damage evolution verification.

Table 1. Material properties of the 3D model [39].

	D (mm)	Tensile strength (MPa)	Cube compressive strength (MPa)	Elasticity modulus (GPa)
CFRP bar	10	1102	-	97
Steel bar	10	677	-	224
Concrete	-	3.4	56.75	45.2

We initially attempted to establish a 3D mesoscopic model based on the 3D macroscopic model. During the modeling process, it was found that the 3D mesoscopic model required an excessively complex mesh and high computational resources, rendering the full calculation process impractical due to the time and memory demands. Moreover, the complexity of the model made it unsuitable for widespread application. After validating the macroscopic model's reliability and considering that the thin-walled geometry of the wall is negligible relative to its planar dimensions [40], we adopted a two-dimensional mesoscopic model to study the material-level damage mechanisms. This model strikes a balance between accuracy and computational efficiency. In the 2D model, shell elements are used to effectively capture the bending and shear characteristics of concrete under plane stress conditions [41], while line elements simulate CFRP bars and steel bars.

Furthermore, considering the CFRP-reinforced shear walls as a four-phase material consisting of spherical aggregate [42] of various sizes, mortar, and CFRP bars and Interface Transition Zones (ITZs) (Figure 2), the mesoscopic numerical model of CFRP-reinforced shear walls was established using Abaqus finite element analysis software. Aggregates with diameters ranging from 5 mm to 20 mm are randomly distributed using the classical "take-and-place" algorithm [43–45], achieving a volumetric fraction of 40% to align with typical concrete compositions. The ITZs were simulated by equally thick thin layers of 1 mm [46] despite the real thickness of 1~5 μm[47–49], to avoid the high computational cost while keeping the acceptable accuracy. Figure 2 is a schematic diagram of the microscopic model of CFRP reinforced shear wall, the bond stress-slip relationship between CFRP bars and concrete was modeled using the connector element in Abaqus, point "D" is used as the displacement collection point.

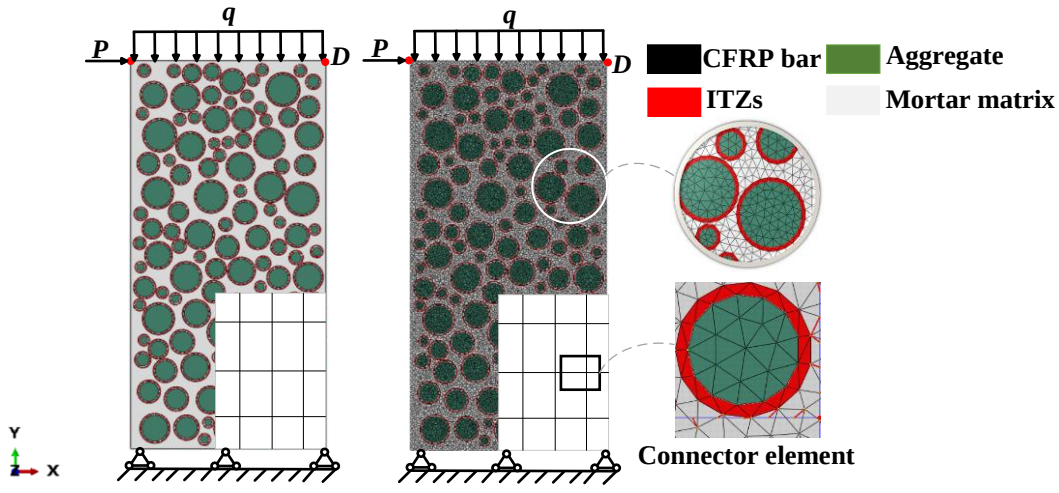

Figure 2. 2D microscopic model of CFRP reinforced shear wall.

In this study, 28 CFRP-reinforced shear walls with different structural lengths of 600 mm, 1200 mm, 1800 mm, and 2400 mm were established to study the seismic performance. According to GB 50010–2010 [50], the horizontal reinforcement ratio was set to three different values: 0.40%, 0.60%, and 0.80%, respectively for each selected structural size. Meanwhile, other important factors, such as the shear span ratio [40], were set to 1, 1.5, and 2, respectively; the height-to-thickness ratio was set to 5, 7.5, and 15, respectively [51]. Table 2 lists the CFRP reinforcement properties used in the model.

Table 2. Material properties of the model.

	D (mm)	Yield strength (MPa)	Ultimate tensile strength (MPa)	Elasticity modulus (GPa)
CFRP bar	8, 10, 16, 20	-	2310.3[#]	143[#]
Steel bar	8, 10, 12, 14	300[^]	420[^]	210[^]

Note: the data with "#" are quoted from [52]; the data with "^" are quoted from test [48].

Figure 3 shows some of the studied cases, where the shear span ratio, concrete strength, and horizontal reinforcement ratio are fixed at 1.0, C30, and 0.40%. The reinforcement conditions and related mechanical parameters of each specimen are shown in Figure 3. The naming convention for the shear wall is "CFRP-size - reinforcement ratio - height-thickness ratio - shear span ratio". For example, CFRP-M-0.40%-7.5-1 represents a specimen with dimensions of 1200 mm × 1200 mm × 160 mm, a horizontal reinforcement ratio of 0.40%, a shear span ratio of λ = 1, and a height-to-thickness ratio of 7.5.

2.2. Constitutive model

To obtain accurate numerical simulation results, the constitutive equations of the four parts must be described in detail and reasonably selected.

2.2.1. Constitutive equations of the CFRP bar

The mechanical behavior of CFRP tendons usually exhibits linear elastic behavior, with high strength and high elastic modulus [18]. The constitutive equation of CFRP materials can be simply described by a linear elastic model (see Figure 4): with E_f and ε_u represent the elasticity modulus and ultimate tensile strain of the CFRP bar, respectively. The performance characteristics of the CFRP bars used in the numerical model are shown in Table 3.

$$\sigma = E_f \varepsilon \ (0 \le \varepsilon \le \varepsilon_u) \quad (1)$$

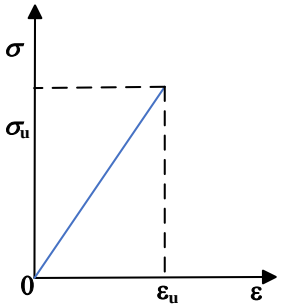

Figure 3. Stress-strain relationship of CFRP bar.

Table 3. Performance properties of CFRP bars.

Property	Typical Value
Tensile strength (MPa)	2310.3[#]
Ultimate tensile strain (%)	1.18^
Elasticity modulus (GPa)	143[#]
Poisson's Ratio	0.27[&]

Note: the data with "&" are quoted from test [53]; The data with "#" are quoted from [52]; the data with "^" are quoted from test [28].

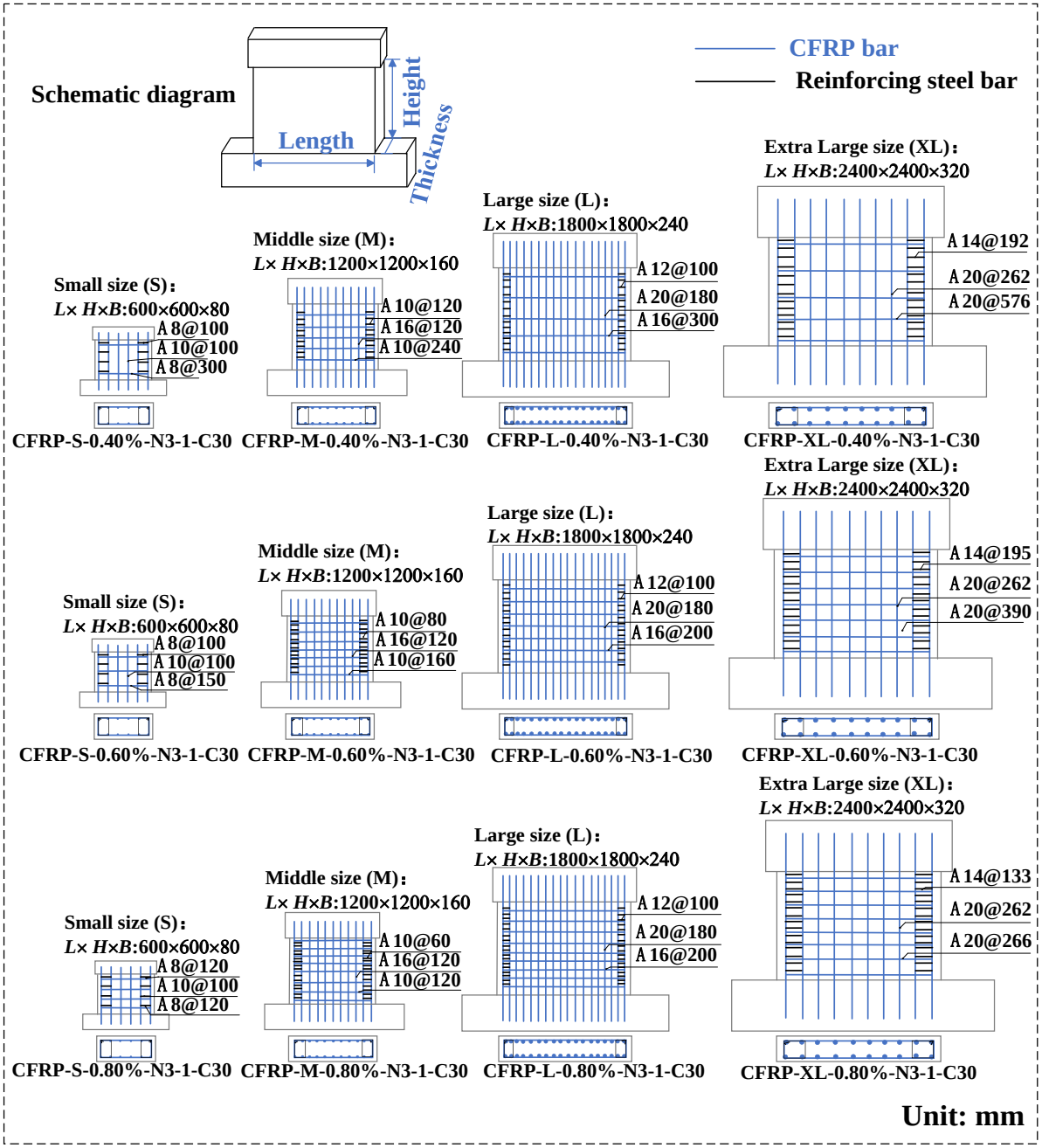

Figure 4. Size and reinforcement arrangement of some specimens.

2.2.2. Constitutive equations of the concrete constituents

The Concrete Damage Plasticity (CDP) model has been effectively utilized in the failure analysis of concrete components [54–56], accurately capturing the nonlinear behavior and damage progression of concrete under both tensile and compressive conditions (Figure 5). Additionally, Jumaa's work [57] suggests that employing the damage plasticity constitutive model is a reasonable and effective approach for studying the size effect in concrete components. Similarly, the damage plasticity model can also be used to describe the mechanical behavior of both the mortar matrix and the ITZ [58]. These studies demonstrate that this model can precisely characterize the mechanical response and damage patterns of concrete across different component sizes. Importantly, the CDP model's ability to integrate both tensile and compressive damage mechanisms aligns with the need to simulate complex failure modes in shear walls, such as combined flexural-shear cracking. As a result, this paper uses the concrete damage plasticity model to represent the mechanical behavior of shear walls. The stress-strain relationship is defined by the following equations:

$$\sigma_t = (1 - d_t)E_0(\varepsilon_t - \varepsilon_t^{pl}) \quad (2)$$

$$\sigma_c = (1 - d_c)E_0(\varepsilon_c - \varepsilon_c^{pl}) \quad (3)$$

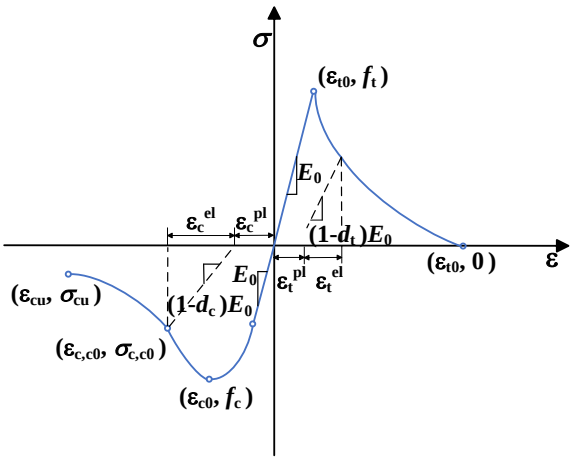

Figure 5. Stress-strain relationship of all concrete constituents described by the CDP model.

Among them, σ_t and σ_c are tensile stress and compressive stress respectively; ε_t and ε_c are tensile strain and compressive strain respectively; E_0 is the initial elastic modulus; d_t and d_c are tensile and compressive damage variables respectively, which quantify the stiffness degradation under tension and compression; ε_t^{pl} and ε_c^{pl} are the equivalent plastic strains in compression and tension respectively, reflecting irreversible deformation during damage evolution.

The key parameters of the CDP model adopted in this study include: θ the expansion angle; γ the eccentricity; β the ratio between the compressive strength between the biaxial and uniaxial loading; and K the ratio between the second stress invariant on the tensile meridian to that of the compressive meridian at the initial yield state, and η the coefficient of viscosity. These parameters collectively govern the yield surface shape, flow potential, and damage hardening/softening behavior of the model. Table 4 gathers the used parameters in the present numerical simulations. These parameters were calibrated based on experimental data from standard concrete material tests and validated against previous studies [59].

Table 4. Other parameters involved in the CDP model [60].

θ	γ	β	K	η
0	0.1	1.16	0.667	0.0005

Aggregates are typically assumed to be linear elastic materials [58], neglecting their nonlinear behavior and irregular shapes. This simplification is justified by their relatively higher stiffness compared to the mortar and ITZ, which dominate the nonlinear response of concrete. Mortars are assumed to be linear elastic materials [61], with their parameters calculated using empirical formulas [62] based on concrete grade and composition. For the ITZs, their properties are generally considered to be between 70% and 85% of those of the mortar [63], and in this study, it was taken as 80%, simplified as thin, isotropic layers. These assumptions are compatible with the CDP model's capability to capture interface weakening effects through damage variables, rather than explicitly modeling microscale heterogeneities. These assumptions balance computational efficiency with model fidelity while preserving the interface weakening mechanisms critical for damage evolution analysis. Table 5 lists the material parameters of all concrete components, including the mass density ρ $(\mathrm{kg/m^3})$, elastic modulus E (GPa), and Poisson's ratio ν for the mortar, ITZ, and aggregates.

Table 5. The used parameters in the CDP model for the CFRP-reinforced shear wall.

	ρ $(\mathbf{kg/m^3})$	E (GPa)	ν
Mortar	$2.20 \times 10^{3\wedge}$	30	$0.16^{\#}$
ITZ	$2.80 \times 10^{3\#}$	24	$0.16^{\#}$
Aggregate	$2.80 \times 10^{3*}$	70*	0.22*

Note: the data with "^" are obtained based on engineering experience; The data with "#" are quoted from [63]; the data with "*" are quoted from test [54].

2.3. Boundary conditions and contact effect

Setting appropriate boundary conditions and determining the type of contact between all components are key to obtaining accurate simulation results through finite element analysis. In the Cartesian coordinate system, all displacement components at the bottom of the CFRP-reinforced shear wall are fixed (i.e., μ_x = 0 and μ_y = 0), effectively simulating the rigid foundation constraints in real-world scenarios. A surface load was applied above the shear wall to simulate the real stress conditions, while a cyclic load was applied at point 'P' at the upper left corner of the shear wall to simulate the earthquake action. Point 'D' was designated as the displacement collection point, as shown in Figure 2. The selection of points 'P' and 'D' was consistent with the locations of the experimental sensors to ensure direct comparability between the simulation and physical test data. The experiment follows displacement control as described in [41], utilizing a reverse cyclic loading protocol, as shown in Figure 6, where three cycles are applied at each lateral displacement ratio (μ_x = 1, 2, 3, 4 … mm) to replicate the cumulative damage effects of multiple earthquake aftershocks.

For simulating the bond stress-slip behavior between CFRP bars and concrete under cyclic loading, the bond stress-slip model proposed by Chen *et al.* [59] is employed (Figure 7). The equations (4)–(5) describe the entire bond stress-slip stage where Equation (1) governs the bond stress under positive

cyclic loading, while equation (2) governs the bond stress under negative cyclic loading. Here, d represents the diameter of the CFRP bar; $\mu = {}^{1}/_{d}$, which represents the ratio of the embedded length to the diameter; f_c represents the concrete strength; β and η are the correction coefficients for rib height, rib width, and rib spacing, respectively. Specific parameter values are provided in [59].

$$\tau = \begin{cases} 117.13\mu^{-0.22}d^{-2.03}f_c\beta\eta s, 0 \le s < s_e^+ \\ 66.50\mu^{-0.83}d^{-1.15}f_c^{0.66}\beta^{0.66}\eta s^{0.32}, s_e^+ \le s < s_u^+ \\ 90.29\mu^{-0.92}d^{-0.98}f_c^{0.50}\beta^{0.50}\eta - f_c\beta H, s_u^+ \le s < s_r^+ \\ 74.98\mu^{-1.38}d^{-0.88}f_c^{0.50}\beta^{0.66}\eta, s > s_r^+ \end{cases} \quad (4)$$

$$\tau = \begin{cases} 82.73\mu^{-0.22}d^{-2.22}f_c\beta\eta s, 0 \le s < s_e^- \\ -27.69\mu^{-0.45}d^{-1.13}f_c^{0.68}\beta^{0.68}\eta|s|^{0.35}, s_e^- \le s < s_u^- \\ -62.31\mu^{-0.79}d^{-0.95}f_c^{0.50}\beta^{0.50}\eta - f_c\beta H, s_u^- \le s < s_r^- \\ -119.03\mu^{-1.36}d^{-1.08}f_c^{0.50}\beta^{0.66}\eta, s > s_r^- \end{cases} \quad (5)$$

For two-dimensional problems, the connector element in Abaqus /Explicit (2020 version) can be used to simulate the bond stress-slip behavior between two structural components. The process began by defining the mathematical expression of the bond stress-slip [59] relationship through a theoretical constitutive model. Subsequently, the connector element was created in Abaqus, and element topology and node mapping were batch-generated using Python scripts. The local coordinate system was configured to ensure consistency in the force-displacement direction. After model completion, mesh sensitivity analysis and experimental data comparisons were conducted to verify the model's robustness.

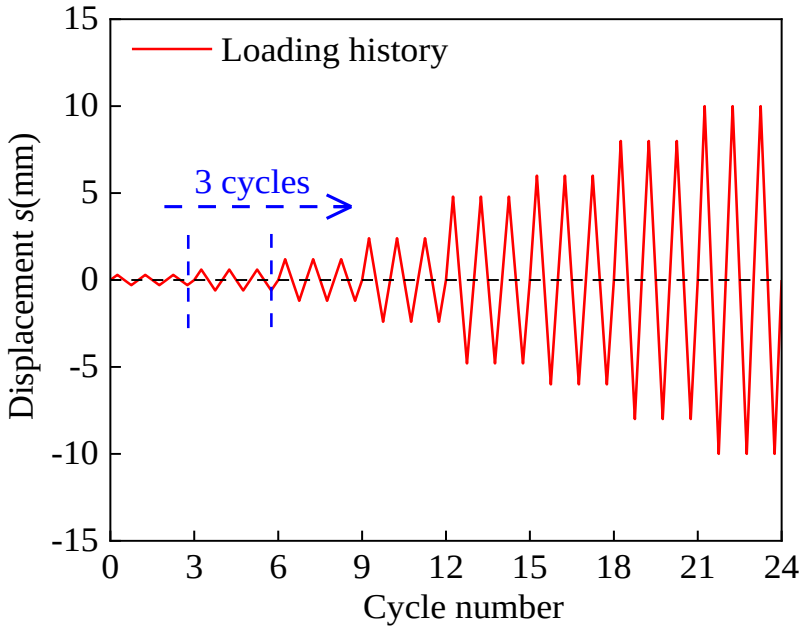

Figure 6. Reversed cyclic loading program.

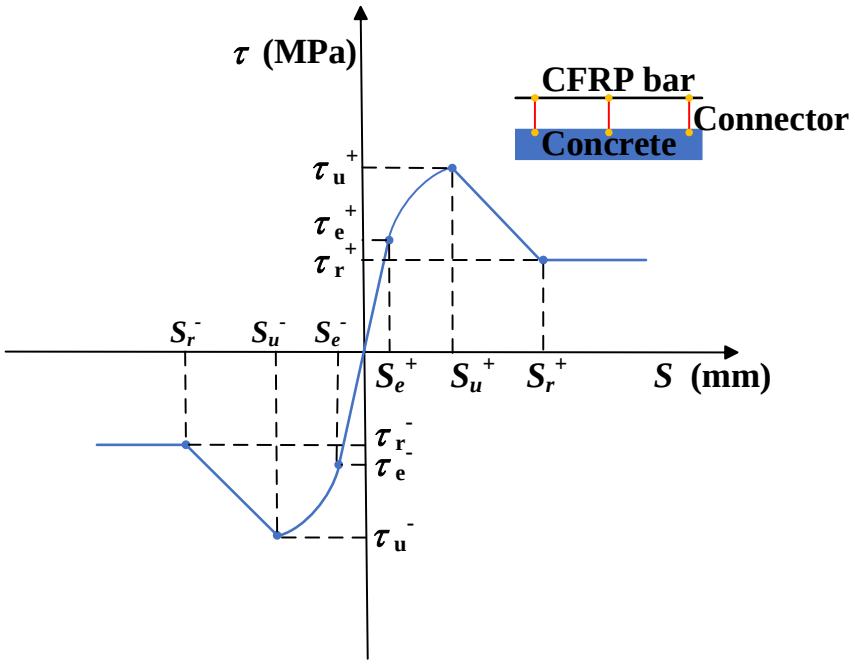

Figure 7. Bond stress–slip relationship between concrete and CFRP bar under reversed cyclic loading.

2.4. Validation of the numerical model

To ensure numerical stability, the grid aspect ratio is strictly controlled within a maximum of 10 [64] to prevent inaccuracies caused by deformation during earthquake simulations. By reproducing the work of Miao *et al.* [65] and comparing the simulation results for different grid sizes with the experimental data, as shown in Figure 8(a)–(b), we found that a 6 mm grid size significantly improved computational efficiency while maintaining accuracy. Therefore, selecting a 6 mm grid size not only ensures the accuracy of the results but also optimizes the utilization of computing resources, achieving a balance between accuracy and efficiency.

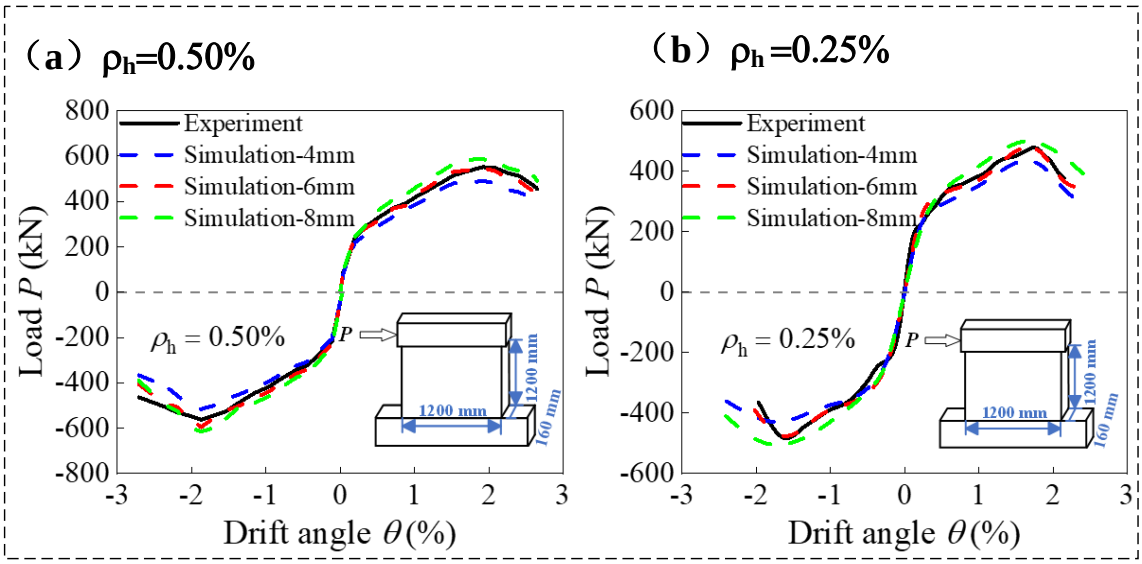

Figure 8. Mesh sensitivity analysis.

To verify the accuracy of the model, the simulation results were compared with those of three available tests [65–67], including two reinforced concrete shear walls and four FRP-reinforced shear walls. The mechanical parameters of the meso-components of concrete and the design parameters of the tested specimens are listed in Tables 6, 7, and 8. Figure 9 presents a comparison between the simulation results and the test results of Looi *et al.* [66], including the failure mode and load-drift angle curves. Clearly, good agreement is observed between the simulation and test results. This indicates that the proposed modeling method can effectively simulate the failure behavior of RC shear walls under cyclic loading.

Figure 10(a)–(b) presents a comparative analysis of the failure modes and load-drift angle curves between the numerical simulations (red/black dashed lines) and the experimental data of Miao *et al.* [65] (blue solid lines), based on the parameter configurations in Table 7. The strong agreement between the experimental and simulation results for basalt fiber-reinforced plastic (BFRP)-reinforced shear walls, along with the similar elastic properties of BFRP and CFRP composites, validates the ability of the microscale model to predict the cyclic failure mechanisms in CFRP-reinforced systems. However, relying solely on Miao *et al.* [65] may not fully substantiate the reliability of the numerical model. Therefore, additional independent experimental comparisons were conducted to enhance the model's credibility and validation. We incorporated the experimental results from Huang *et al.* [67] and extracted independent validation data for comparison with the present model (Figure 11). The experimental study used CFRP-reinforced concrete shear walls, similar to the model established in this paper. A quantitative comparison showed that the deviation in the load-displacement response was less than 5%, systematically confirming the prediction accuracy of the present model across different design parameters.

In addition, the specimens considering the effect of bond stress-slip (red dashed line) and the specimens not considering the effect of bond stress-slip (black dashed line) were compared. The results showed that the specimens considering bond stress-slip were closer to the experimental results, indicating that bond stress-slip has a significant effect on the seismic performance of shear walls. It reflects the degradation of the bond between reinforcement and concrete, which can occur due to large cyclic loads or long-term effects, impacting the wall's overall seismic response. Without bond slip, the shear wall's strength and stiffness are often overestimated since the full contribution of reinforcement is assumed, ignoring potential slippage that might reduce load transfer.

Table 6. The used parameters in Looi *et al.* [66] for reinforced concrete shear wall.

	$\boldsymbol{\rho}$ (kg/m^3)	$\boldsymbol{d}$ (mm)	$\boldsymbol{E}$ (GPa)	$\boldsymbol{\nu}$
Steel bar	1.9×10$^{3\&}$	10	207.2$^{\&}$	0.30$^{\&}$
Mortar	2.20 × 10$^{3\wedge}$	-	21.6$^{\&}$, 19.8$^{\&}$	0.16$^{\#}$
ITZ	2.80 × 10$^{3\#}$	-	16.95^{a},14.85^{a}	0.16$^{\#}$
Aggregate	2.80 × 10^{3*}	-	70*	0.22*

Note: the data with "&" are quoted from test [66]; The data with "^" are obtained based on engineering experience; The data with "#" are quoted from [63]; The data with "a" are quoted from test [40]; The data with "*" are quoted from test [54].

Table 7. The used parameters in Miao *et al.* [65]. for BFRP-reinforced shear wall.

	ρ (kg/m^3)	d (mm)	E (GPa)	ν
BFRP bar	1.9×10^{3}[&]	8	46.50[a]	0.27[&]
Mortar	2.20×10^{3}[^]	-	42.26[a]	0.16[#]
ITZ	2.80×10^{3}[#]	-	33.81[a]	0.16[#]
Aggregate	2.80×10^{3}[*]	-	70[*]	0.22[*]

Note: the data with "[&]" are quoted from test [53]; The data with "^" are obtained based on engineering experience; The data with "[#]" are quoted from [63]; The data with "[a]" are quoted from test [59]; The data with "*" are quoted from test [54].

Table 8. The used parameters in Huang *et al.* [67] for CFRP-reinforced shear wall.

	ρ (kg/m^3)	Layers of CFRP	d (mm)	E (GPa)	ν
CFRP bar	1.6×10^{3}[&]	3, 4	-	122.69[*],121.76[*]	0.27[&]
Steel bar	7.85×10^{3}[^]	-	6, 10	196.87[*],203.48[*]	0.30[^]
Mortar	2.20×10^{3}[&]	-	-	25[a]	0.20[a]
ITZ	2.80×10^{3}[&]	-	-	22[a]	0.20[a]
Aggregate	2.80×10^{3}[&]	-	-	70[a]	0.20[a]

Note: the data with "[&]" are quoted from test [59]; The data with "^" are obtained based on engineering experience; The data with "[a]" are quoted from test [68]; The data with "*" are quoted from test [67].

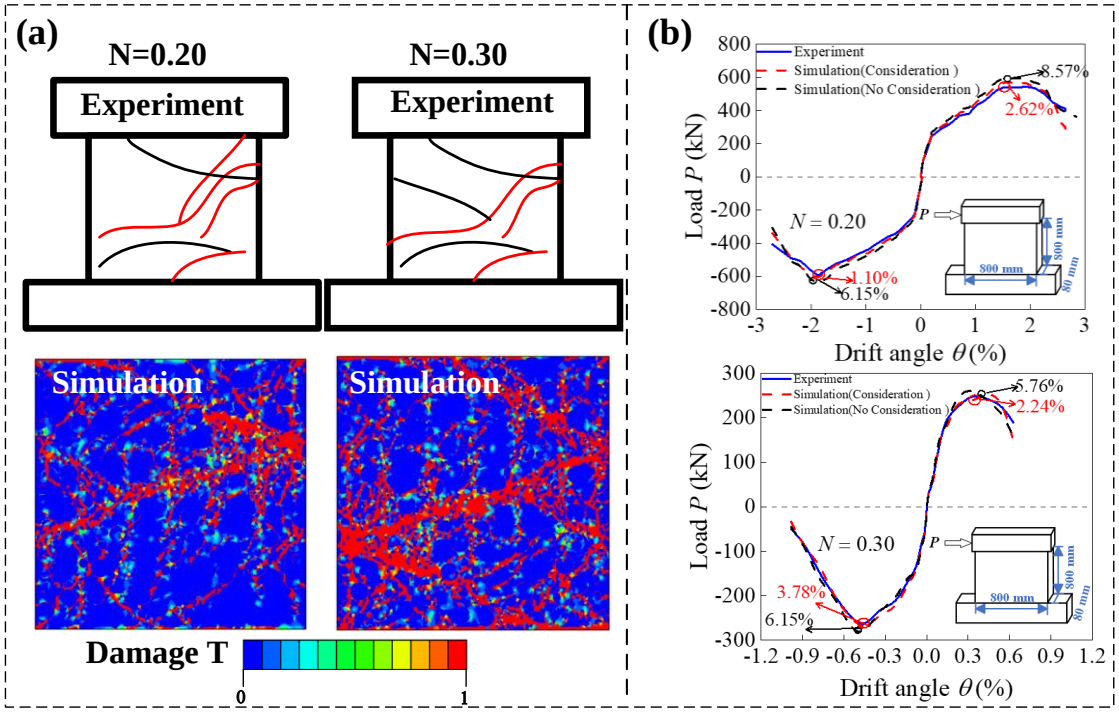

Figure 9. Comparison between the experiment and simulation by Looi *et al.* [66] **(a)** failure mode; **(b)** skeleton.

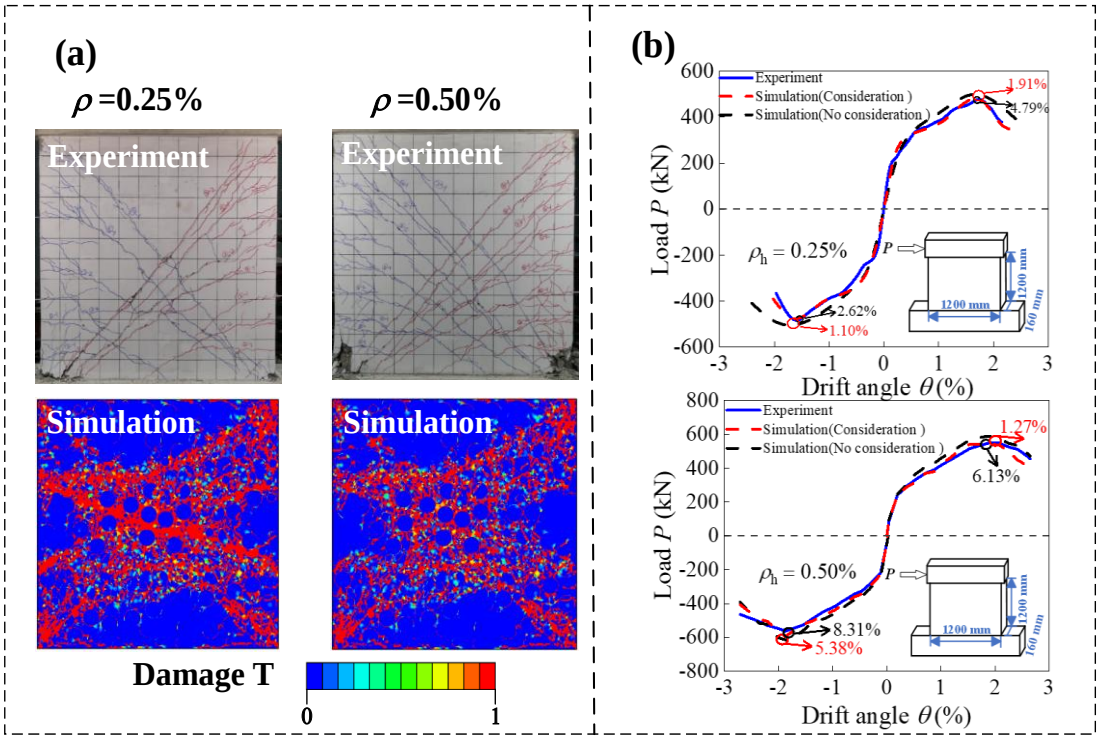

Figure 10. Comparison between the experiment and simulation by Miao *et al.* [65]: **(a)** failure mode; **(b)** skeleton.

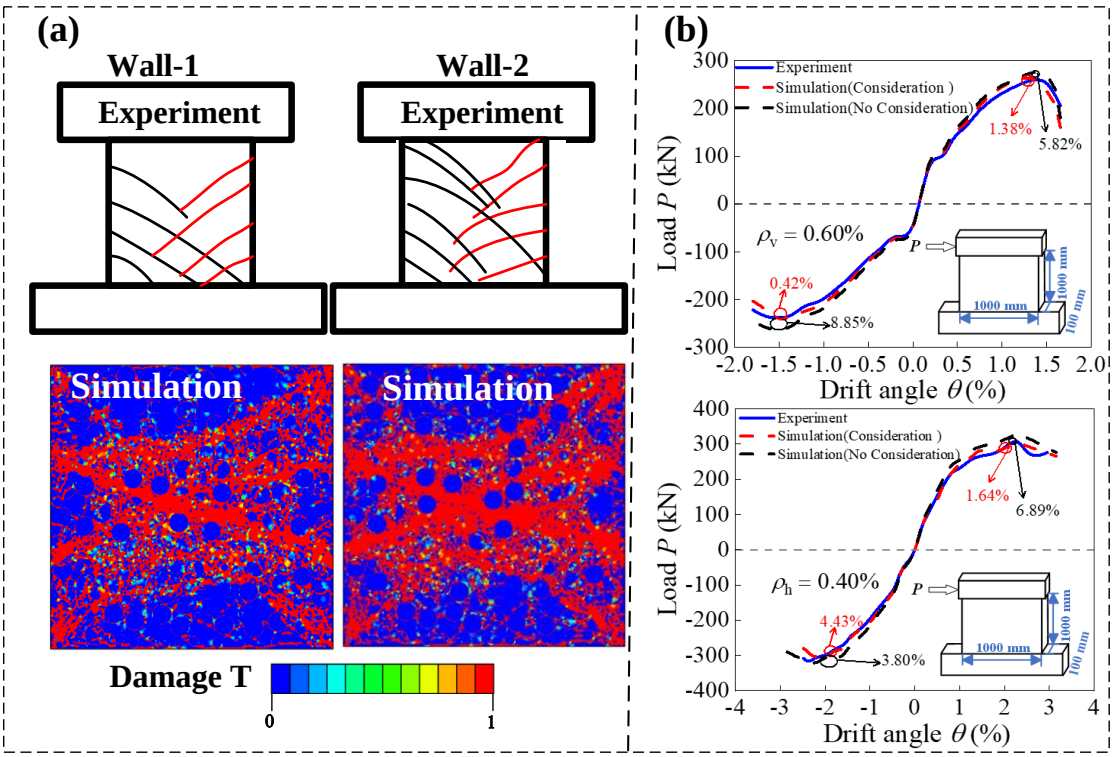

Figure 11. Comparison between the experiment and simulation by Huang *et al.* [67]: **(a)** failure mode; **(b)** skeleton.

3. Meso-scale simulation results and analysis

3.1. Failure mode

The failure mode of the shear wall changes similarly with the shear wall size, horizontal reinforcement ratio, shear span ratio and height-to-thickness ratio, so a medium shear wall with a horizontal reinforcement ratio of 0.80%, a shear span ratio of 1, and a height-to-thickness ratio of 7.5 was selected for the analysis. As shown in Figure 12, the shear wall exhibits a shear failure, and oblique cracks (about 45°) are distributed throughout the wall as the loading system progresses.

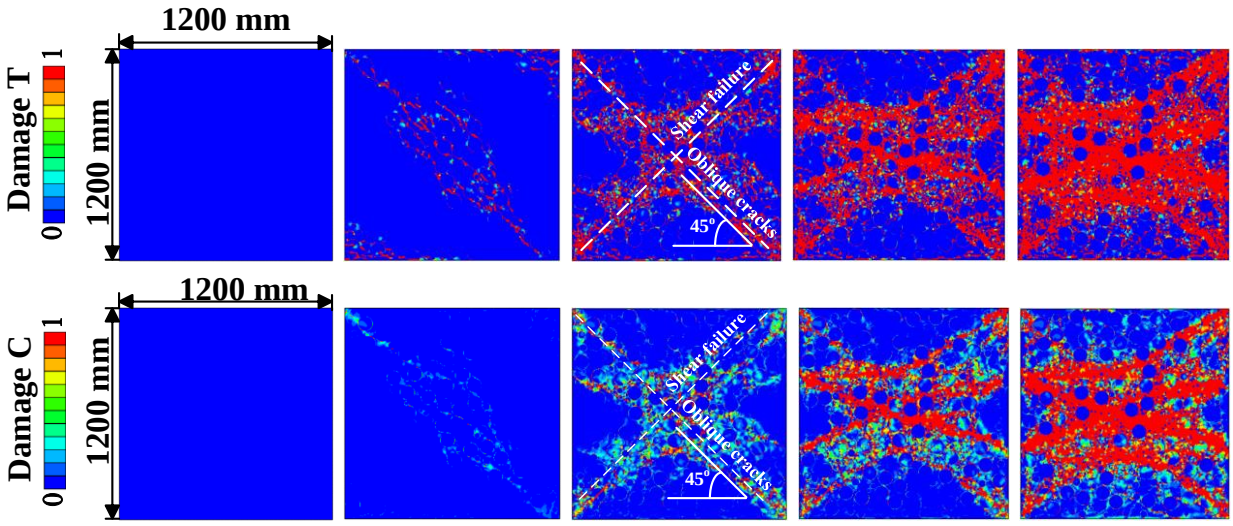

Figure 12. Shear wall failure mode.

3.2. Load-Displacement curves

Figure 13 shows the shear wall skeleton curves with horizontal reinforcement ratios of 0.40% to 0.80%, shear span ratios of 1.0 to 2.0, and height-to-thickness ratios of 5 to 7.5. As can be seen from Figure 13, the peak loads of all specimens decrease with the increase of the shear span ratio, and the shear span ratio has a great influence on the seismic bearing capacity of the shear wall. At the same time, the shear bearing capacity of the shear wall increases with the increase of the horizontal reinforcement ratio. In addition, the shear bearing capacity of the shear wall increases with the decrease of the height-to-thickness ratio, indicating that the thicker shear wall has better shear bearing capacity and energy dissipation capacity.

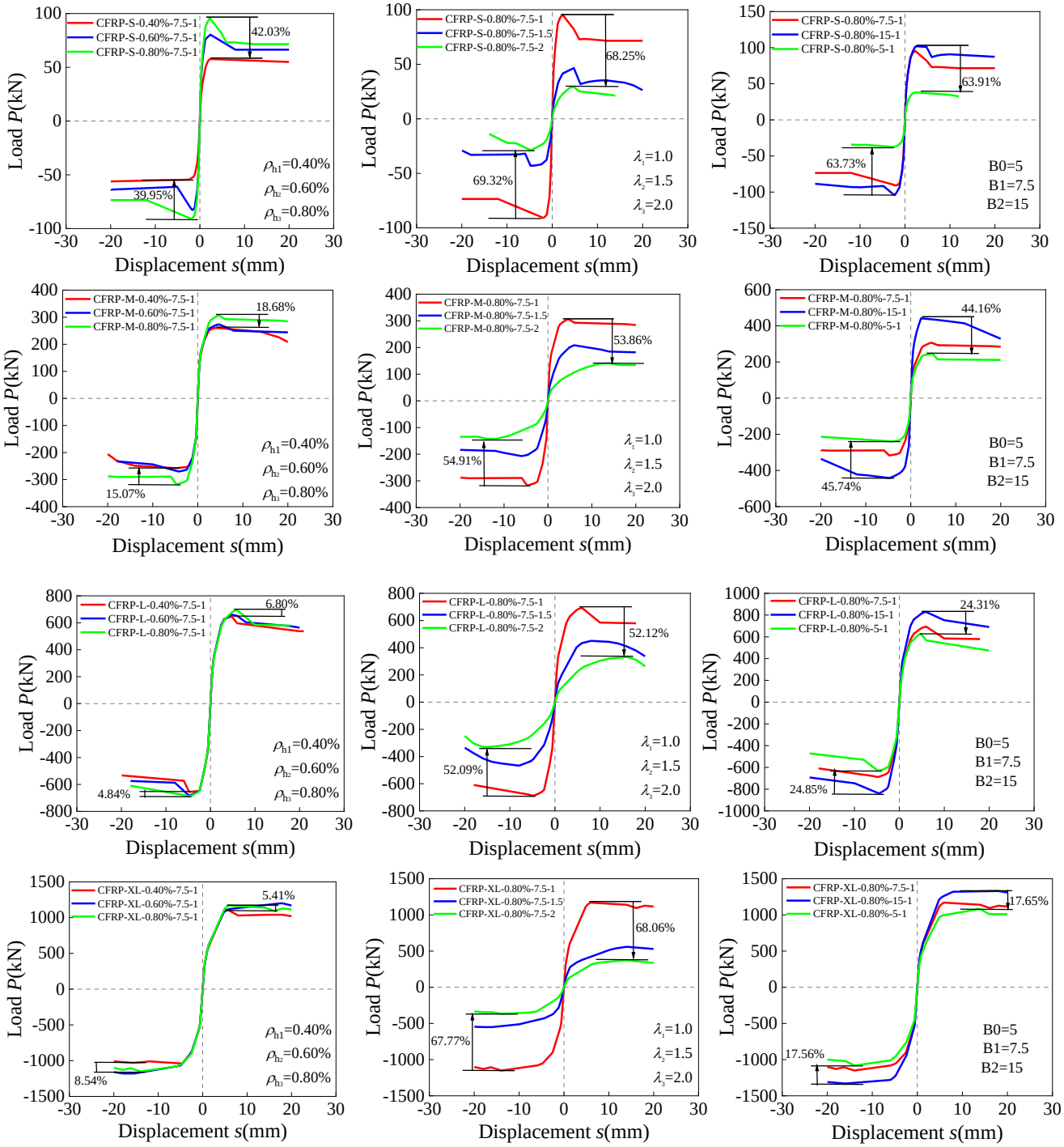

Figure 13. Skeleton curves of CFRP-reinforced shear walls.

3.3. Deformation capacity

For CFRP-strengthened walls, the ductility coefficient (μ) is defined as [69]:

$$\mu = \frac{\Delta_u}{\Delta_e} \tag{6}$$

where Δ_e represents the elastic displacement corresponding to the point at which the concrete enters the plastic zone, or begins to exhibit plastic deformation due to compressive stress or cracking. It is

calculated by the energy equivalent method [70]. Δ_u denotes the ultimate displacement, and the ultimate strength is expressed as 0.85Pmax.

Figure 14(a) shows the combined effects of structural size and horizontal reinforcement ratio on the ductile behavior of CFRP-reinforced shear walls. The results indicate that as the wall length increases from 600 mm to 2400 mm, the ductility coefficients of the specimens with ρ_h = 0.40%, 0.60%, and 0.80% decrease by 17.57%, 21.52%, and 22.56%, respectively, due to the size effect of the CFRP-reinforced shear wall. The larger the shear wall, the more pronounced the stress localization and crack propagation, especially in areas with lower restraint [67]. In addition, increasing ρ_h can mitigate this trend to some extent. For the 1200 mm-long wall, the ductility coefficient increases by 5.04% when the reinforcement ratio increases from 0.40% to 0.60%. However, since the horizontal CFRP bars primarily resist shear forces rather than bending deformation, a higher horizontal reinforcement ratio, although effective in controlling crack distribution, cannot fully prevent the accumulation of tensile damage in CFRP bars under large displacements [67]. Therefore, the horizontal reinforcement ratio can only mitigate the size effect to a limited extent.

Figure 14(b) shows the effects of the shear span ratio and structural size on the ductile behavior of CFRP-reinforced shear walls. The results indicate that as the wall length increases from 600 mm to 2400 mm, the ductility coefficient decreases by 22.56%, 22.86%, and 26.07%, respectively, indicating that an increase in size exacerbates the ductility degradation of the shear wall. As the shear span ratio increases, the failure mode of the shear wall shifts from shear-dominant to bending-dominant, while a larger structural size exacerbates the strain incompatibility between CFRP bars and concrete, accelerating interface debonding [41]. Notably, increasing the shear span ratio can significantly enhance the ductility of the shear wall. For example, for a shear wall with a length of 1200 mm, increasing the shear span ratio from 1 to 1.5 raises the ductility coefficient by 42.64%, confirming that the shear span ratio is more effective than other parameters in regulating deformation performance.

Similarly, Figure 14(c) analyzes the effects of the height-to-thickness ratio and structural size on the ductile behavior of CFRP-reinforced shear walls. It is evident that as the wall length increases from 600 mm to 2400 mm, the ductility coefficient of the samples with B = 15, 7.5, and 5 decreases by 16.08%, 22.56%, and 24.87%, respectively. This phenomenon illustrates the interaction between the size effect and the height-to-thickness ratio. In addition, reducing the height-to-thickness ratio can enhance deformation capacity. When the height-to-thickness ratio decreases from 15 to 7.5, the ductility coefficient of the 600 mm wall increases by 14.37%. A lower height-to-thickness ratio results in a larger cross-sectional area, which can delay the spalling of the concrete cover and improve stress transfer efficiency at the CFRP bar–concrete interface [71].

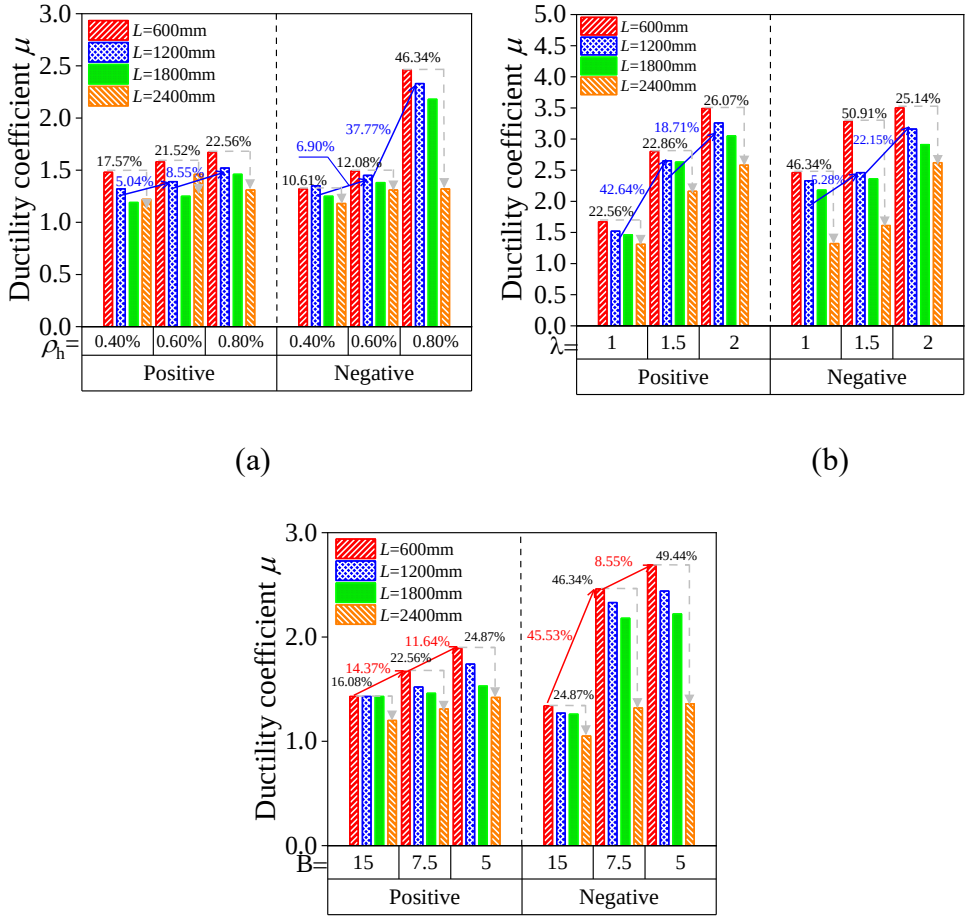

Figure 14. Ductility coefficient: **(a)** horizontal reinforcement ratio; **(b)** shear span ratio; **(c)** height-thickness ratio.

3.4. Stiffness degradation

The secant stiffness K_i [72] is defined by the following expression:

$$K_i = \frac{|+P_i|+|-P_i|}{|+\Delta_i|+|-\Delta_i|} \tag{7}$$

where $+P_i$ and $-P_i$ represent the loads in the positive (tension) and negative (compression) directions, respectively, and $+\Delta_i$ and $-\Delta_i$ are the corresponding displacements.

Figure 15 presents the stiffness degradation curves of shear walls with varying sizes, horizontal reinforcement ratios, shear span ratios, and height-to-thickness ratios. These curves indicate that, during the initial stage of loading, the stiffness of the specimens decreases significantly due to rapid wall cracking and the resulting plastic deformation of the concrete. Larger specimens exhibit higher initial stiffness. For example, the initial stiffness of the wall with a length of 2400 mm is approximately four times that of the 600 mm wall. However, the residual stiffness of the wall does not change significantly with variations in size.

The main function of horizontal reinforcement is to resist shear forces and enhance ductility, rather than increase bending stiffness [65]. Therefore, changes in horizontal reinforcement do not significantly affect the overall stiffness degradation trend. In contrast, the shear span ratio and height-to-thickness ratio have a significant impact on the wall's stiffness degradation. Specifically, as shown in Figures 15(b) and 15(c), a

smaller shear span ratio enhances the contribution of the arching effect [67], improving the overall stiffness retention rate, while a larger shear span ratio increases bending deformation, accelerating stiffness decline. Similarly, thinner walls exhibit poorer seismic performance because they are more susceptible to shear failure. In this case, the reduced cross-sectional area lowers overall stiffness and shear strength, making the structure more vulnerable to rapid deterioration under cyclic loading [71].

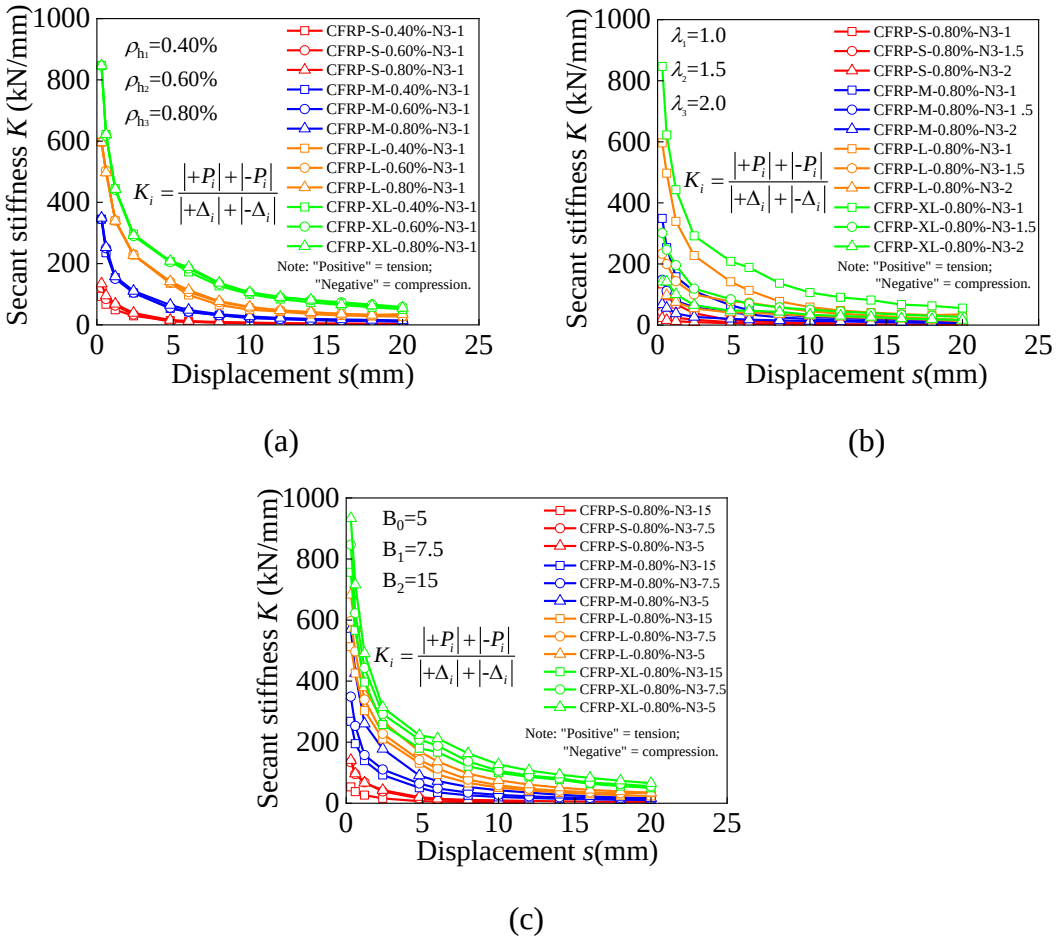

Figure 15. Stiffness degradation: **(a)** horizontal reinforcement ratio; **(b)** shear span ratio; **(c)** height-thickness ratio.

3.5. Strength degradation

For CFRP-reinforced walls, the strength degradation coefficient η can be defined by the following formula [73]:

$$\eta = \frac{P_{\mathrm{n}}}{P_{\max}} \tag{8}$$

P_{n} represents the maximum load in each cycle of the hysteresis curve, while $P_{\max}$ represents the maximum load during the entire hysteresis process.

Since the strength degradation behavior of shear walls under positive loads is similar to that under negative loads, this paper focuses on strength degradation under positive load to avoid repeated analysis. Figure 16 shows the strength degradation curves of shear walls with different sizes, horizontal

reinforcement ratios, shear span ratios, and height-to-thickness ratios. It is clearly observed that the strength degradation coefficient gradually increases during the initial loading stage. After reaching the maximum strength, the coefficient gradually decreases and approaches a smooth curve.

The increase in horizontal reinforcement ratio enhances the confinement effect of concrete, delays the propagation of cracks, and increases the strength degradation coefficient [67]. Therefore, walls with larger reinforcement ratios exhibit a slower strength degradation rate, as shown in Figure 16(a). In addition, the shear span ratio significantly affects strength degradation, as shown in Figure 16(b). A reduction in shear span ratio increases the contribution of shear force relative to the bending effect [67], causing the shear wall to fail more quickly and cracks to develop rapidly, leading to a faster strength decline. In contrast, walls with larger shear span ratios experience slower bending deformation, resulting in a slower strength decline.

Similarly, the height-to-thickness ratio plays a key role in strength degradation. Walls with large height-to-thickness ratios have smaller cross-sectional areas to resist shear forces [71], making them more susceptible to cracking under cyclic loading, which results in relatively rapid strength degradation, as shown in Figure 16(c). Therefore, as the height-to-thickness ratio increases, the structural integrity of the wall deteriorates more quickly.

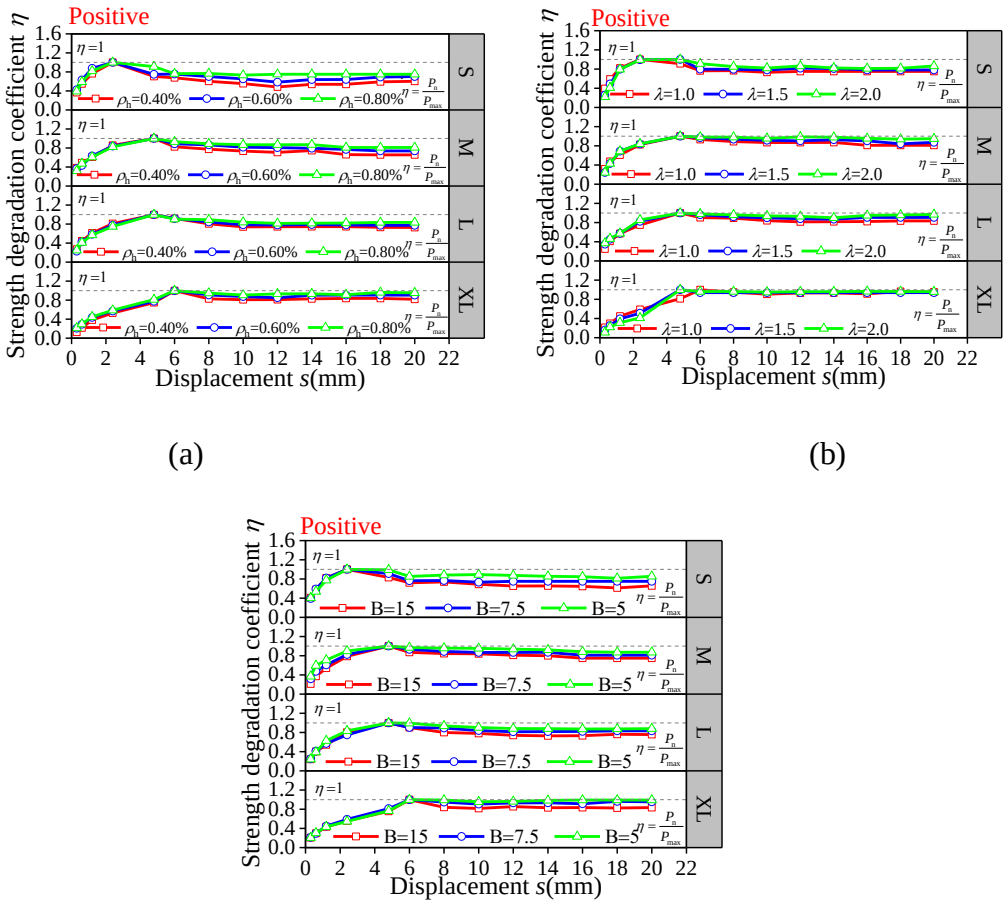

Figure 16. Strength degradation: **(a)** horizontal reinforcement ratio; **(b)** shear span ratio; **(c)** height-thickness ratio.

3.6. Energy dissipation capacity

Energy dissipation capacity is a crucial parameter for assessing the seismic performance of shear walls, as it reflects the structure's toughness and ductility in resisting damage under cyclic loading. The energy dissipation coefficient ζ [74], as depicted in Figure 17, is defined by the following equation:

$$\zeta = \frac{S_{ABC+CEA}}{S_{OBD+OEF}} = \frac{E}{S_{OBD+OEF}} \quad (9)$$

Here, $S_{ABC+CEA}$ represents the area of the hysteresis loop (the shaded area in Figure 17), which corresponds to the cumulative dissipated energy *E*. Similarly, $S_{OBD+OEF}$ denotes the combined area of triangles OBD and OEF.

Figure 18 illustrates the effect of the energy dissipation coefficient as a function of the horizontal reinforcement ratio, shear span ratio, and height-to-thickness ratio. Increasing the horizontal reinforcement ratio enhances the internal confinement effect of the shear wall, delays crack propagation, and maintains structural integrity under cyclic loading [27], significantly improving the shear wall's ability to dissipate energy, as shown in Figure 18(a). Therefore, walls with higher horizontal reinforcement ratios exhibit a more stable increase in cumulative dissipated energy, indicating that they have a stronger ability to absorb seismic energy and are less likely to fail prematurely.

A decrease in the shear span ratio promotes shear failure of the shear wall [51], limiting its deformation and reducing the wall's ability to dissipate energy. Therefore, for shear walls with lower shear span ratios, as shown in Figure 18(b), the cumulative dissipated energy increases more slowly, indicating that such walls have lower energy absorption efficiency. Increasing the thickness of the wall gives it greater shear resistance and better confinement [51], allowing it to withstand greater inelastic deformation before failure. This enables it to absorb and dissipate more seismic energy, helping to improve the overall elasticity of the structure. As shown in Figure 18(c), the accumulated dissipated energy increases faster for shear walls with a smaller height-to-thickness ratio.

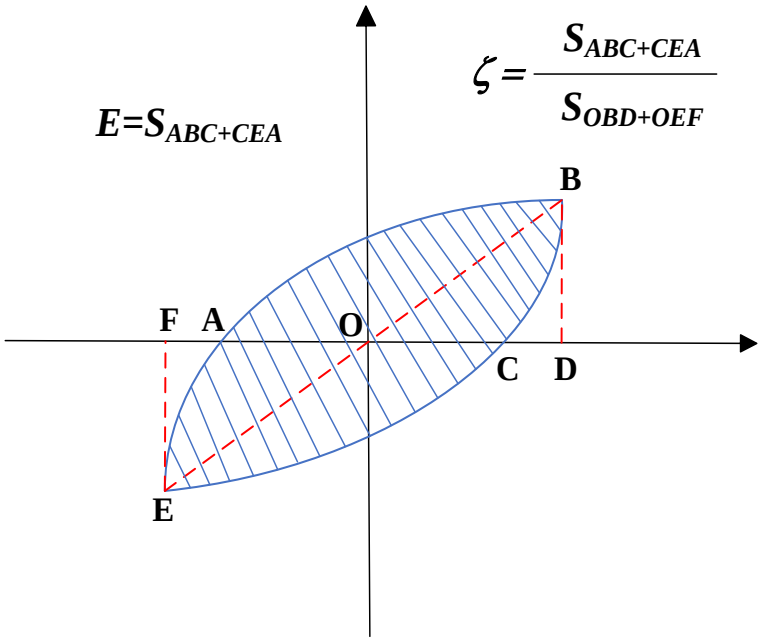

Figure 17. Calculation of ζ and E.

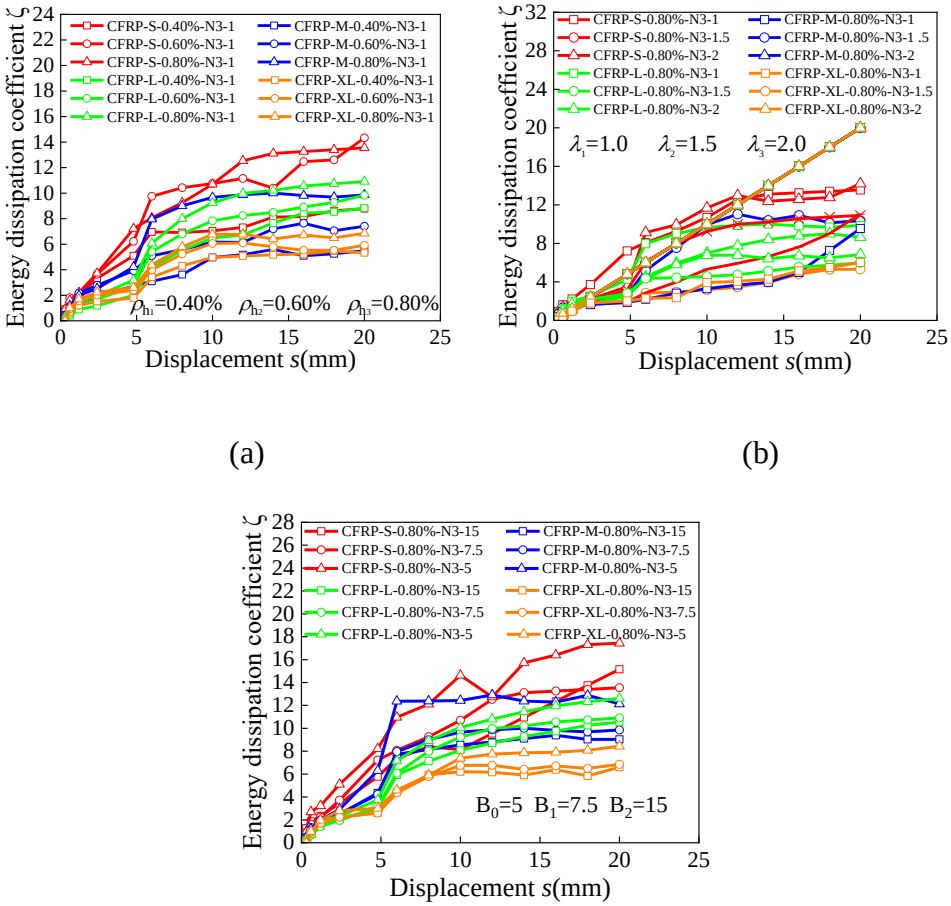

Figure 18. Energy dissipation coefficient ζ: **(a)** horizontal reinforcement ratio; **(b)** shear span ratio; **(c)** height-thickness ratio.

3.7. Hysteresis residual deformation

Hysteretic residual deformation is an important deformation index for evaluating the seismic performance of shear walls, which mainly reflects their plastic deformation capacity and energy dissipation capacity under repeated loads such as earthquakes. It can be described by the hysteretic residual deformation ratio. For CFRP-reinforced walls, the hysteretic residual deformation [75] ratio γ can be defined by the following formula:

$$\gamma = \frac{s_{\mathrm{n}}}{s_{\max}} \tag{10}$$

with s_{n} represents the residual deformation of each cycle in the hysteresis process, and $s_{\max}$ represents the maximum residual deformation in the entire hysteresis process.

Figure 19 shows the residual deformation rate curves corresponding to shear walls of different sizes, horizontal reinforcement ratios, shear span ratios, and height-to-thickness ratios. Smaller shear walls exhibit smaller overall deformations, allowing them to redistribute stress more quickly while maintaining structural integrity [28]. Therefore, smaller shear walls have smaller hysteretic residual

deformations and relatively stronger plastic deformation capacity, enabling them to maintain good ductility under large earthquakes.

Increasing the horizontal reinforcement ratio of shear walls provides greater support during the plastic deformation stage, effectively delaying structural yielding, reducing the accumulation of residual deformations [75], and enabling the shear walls to maintain higher structural performance after the plastic deformation stage, as shown in Figure 19(a). The larger the shear span ratio, the more pronounced the bending behavior [67], allowing for larger deformations to occur without immediate failure. This enables the wall to absorb more energy and results in smaller residual deformations after an earthquake. As shown in Figure 19(b), the wall with a larger shear span ratio has smaller hysteretic residual deformations and a stronger deformation capacity. Thicker walls generally have higher stiffness, which limits their deformation under lateral loads, reducing their energy dissipation capacity [51]. This results in relatively weaker energy absorption performance, making the structure more susceptible to failure in the later stages of loading. As shown in Figure 19(c), the smaller the height-to-thickness ratio, the smaller the deformation under seismic loads and the smaller the hysteretic residual deformation.

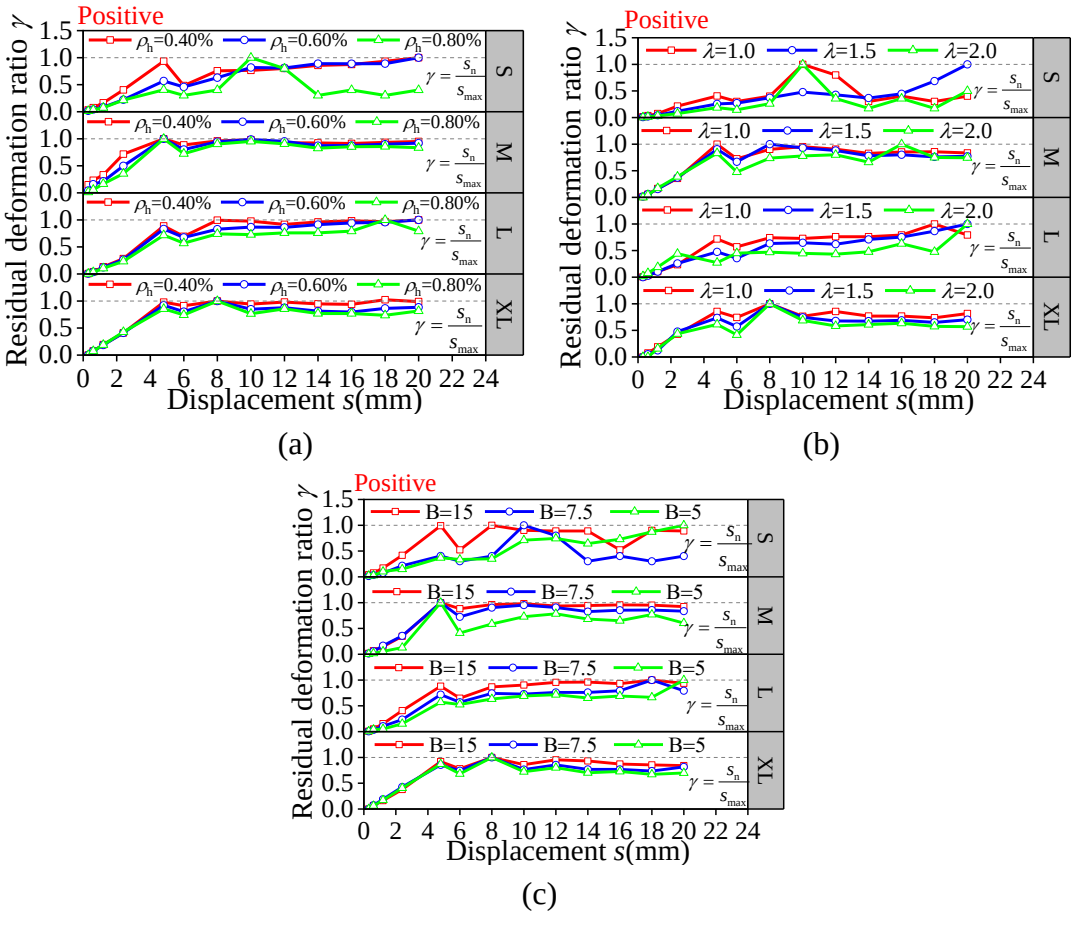

Figure 19. Residual deformation ratio γ: **(a)** horizontal reinforcement ratio; **(b)** shear span ratio; **(c)** height-thickness ratio.

4. Size effect analysis

4.1. Main factors that influence the size effect

A systematic analysis of shear capacity evolution was conducted through parametric evaluation of nominal shear strength (τ) using the relationship [76]:

$$\tau = \frac{P}{LT} \tag{11}$$

where P represents peak horizontal load, L denotes wall length, and T specifies cross-sectional thickness. The bilateral loading symmetry observed in Figure 20 permits focused examination of positive loading behavior.

As the size increases from 600 mm to 2400 mm, a clear decrease in shear strength can be observed. As shown in Figure 20(a), the nominal shear strength of the specimens with horizontal reinforcement ratios of 0.40% and 0.80% decreased by 29.03% and 25.76%, respectively. This difference indicates that increasing the horizontal reinforcement ratio can mitigate the size effect by improving crack distribution [65].

Figure 20 (b) reveals the effect of shear span ratio on the size effect. It can be seen that the nominal shear strength of the shear wall specimens with shear span ratios of 1 and 2 decreased by 25.76% and 9.93%, respectively, indicating that the increase in shear span ratio can effectively weaken the size effect. The increase in shear span ratio can effectively change the moment redistribution mode and promote structural behavior dominated by bending rather than shear [67]. Conversely, an increase in the height-to-thickness ratio reduces the relative thickness of the shear wall [51], diminishing its cross-sectional bending capacity and weakening the confinement effect, thereby accelerating concrete failure. As shown in Figure 20(c), the nominal shear strength of shear wall specimens with height-to-thickness ratios of 5 and 15 decreased by 20.90% and 30.85%, respectively, indicating that a higher height-to-thickness ratio exacerbates the size effect.

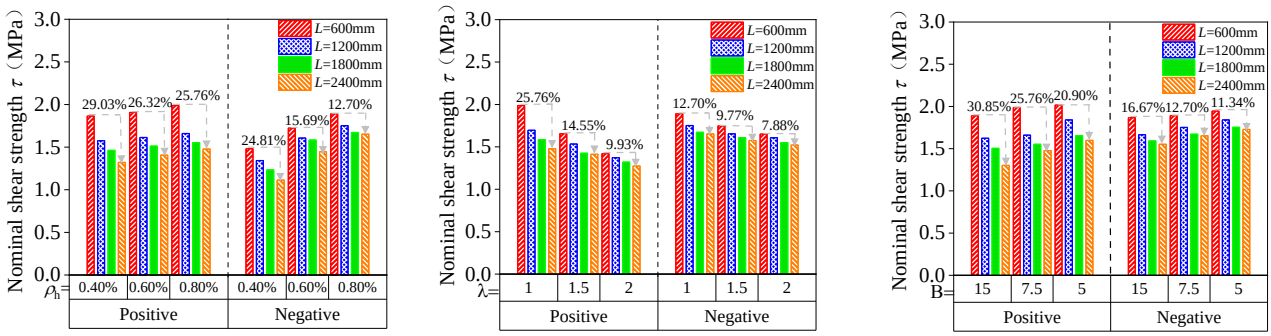

(a) (b) (c)

Figure 20. The size effect: **(a)** horizontal reinforcement ratio; **(b)** shear span ratio; **(c)** height-thickness ratio.

4.2. Modification of the size effect law

As established in Section 4.1, CFRP-reinforced shear walls demonstrate significant size-dependent shear failure characteristics modulated by three critical parameters: 1) shear span ratio (λ), 2) horizontal reinforcement ratio (ρ_h), and 3) height-to-thickness ratio ($B = H/t$). While Jin *et al.*'s foundational model (Equation. 12–17) [77] successfully incorporates λ and ρ_h through the φ' and β terms, it neglects the pivotal role of B in governing: (1) Flexural-shear interaction through neutral axis migration; (2) Out-of-plane stability via reduced buckling resistance; (3) Stress redistribution capacity under cyclic loading.

$$\tau_c' = V_u \varphi' \gamma \beta \tag{12}$$

$$V_u = \frac{V_0 - V_{d\to\infty}}{1 + \frac{d}{d_0}} + V_{d\to\infty} \tag{13}$$

$$\varphi' = \begin{cases} 1, \rho_h \le \rho_{h,min} \; and \; \lambda \le 0.5 \\ (\varphi_0 - 1)\tanh\left[\alpha_1(\rho_h - \rho_{h,min}) + \alpha_2(\lambda - 0.5)\right] + 1, \rho_h > \rho_{h,min} \; or \; \lambda > 0.5 \end{cases} \tag{14}$$

$$\varphi_0 = \frac{0.39 \times (10 f_t)^{0.57}}{\frac{V_0 - V_{d\to\infty}}{1 + \frac{d}{d_0}} + V_{d\to\infty}} \tag{15}$$

$$\gamma = e^{n\left[a\left(\frac{L}{L_{min}}\right)+b\right]} \tag{16}$$

$$\beta = \frac{1}{0.5 + \lambda} \tag{17}$$

To address this theoretical gap, as illustrated in Figure 21, we propose a new dimensionless parameter β_0 (Equation. 18), which incorporates the effects of B into the original formulation:

$$\beta_0 = \beta - 0.02B + 1.15 = \frac{1}{0.5 + \lambda} - 0.02B + 1.15 \tag{18}$$

As demonstrated in Table 9, the enhanced model reduces prediction errors from 15.62% (original) to 5.80% for walls, while maintaining computational efficiency. Compared with the existing formula, its advantages can be seen in Table 9.

Table 9. Advantages over existing formulas.

Feature	Jin *et al.* [77]	Proposed Model
B ($\frac{H}{t}$) Consideration	None	β_0
Error (B = 15)	15.62%	5.80%
Fracture Energy Link	Empirical	Mechanistic

This theoretical advancement bridges a critical gap in size effect modeling by incorporating geometric proportionality effects, thereby enabling reliable predictions for high-rise prototypes of modern slender CFRP-reinforced walls. The modified formulation retains backward compatibility while extending its applicability to configurations with B ≤ 15, addressing a key limitation in current design codes.

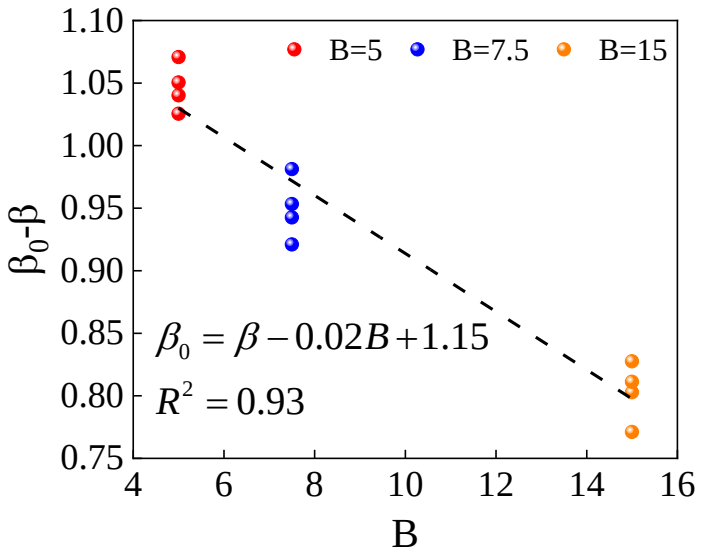

Figure 21. The relationship between height-to-thickness ratio and β_0.

4.3. Comparison with size effect law

The predictive capability of the size effect law was evaluated by comparing the simulation results of 28 CFRP-reinforced shear walls with the theoretical size effect law. The verification process, shown in Figure 22, demonstrates a strong correlation between the numerical simulation and the analytical prediction, while statistical parameters confirm the model's accuracy and stability across all dimensional scales.

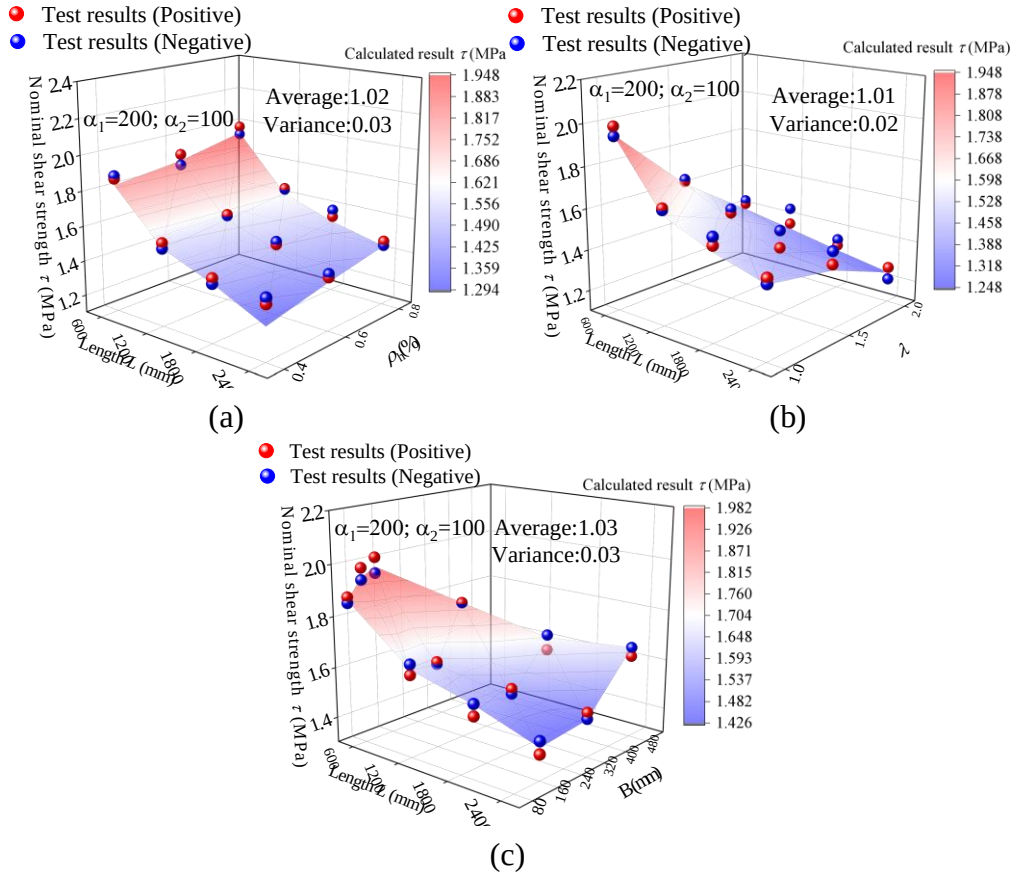

Figure 22. The size effect: **(a)** horizontal reinforcement ratio; **(b)** shear span ratio; **(c)** height-thickness ratio.

Current international design standards for FRP-reinforced shear walls remain limited, with only ACI 440.11–22 [78] and CSA S806–2012 [79] providing explicit shear capacity formulations:

$$V = V_c + V_f \tag{19}$$

Where concrete contribution (V_c) and FRP reinforcement contribution (V_f) are calculated differently:

(1) ACI 440.11–22:

$$V_c = \frac{2}{5}\sqrt{f_c'}\,b_w(kd) \tag{20}$$

$$V_f = \frac{A_{fv}f_{fv}d}{s}\ (f_{fv} = 0.004E_f) \tag{21}$$

(2) CSA S806–2012:

$$V_c = 0.05\lambda\varphi_c k_s k_m k_r k_a \sqrt[3]{f_c'}\,b_w d_v \tag{22}$$

$$V_f = \frac{0.4\varphi_F A_{fv}f_{fv}d}{s}\ (f_{fv} = 0.005E_f) \tag{23}$$

Critical parameter definitions include: f_c' = concrete compressive strength, b_w = web width, d = effective depth, k = neutral axis depth ratio, A_{fv} = FRP reinforcement area, s = bar spacing, E_f = FRP elastic modulus, φ_c/ φ_F = material resistance factors.

Reliability evaluation using the safety index (SI = $\tau_{test}/\tau_{calculated}$) [80] revealed limitations in current code provisions. Figure 23 shows that the SI value decreases as wall length increases, potentially dropping below 0.85, indicating that code predictions may be unsafe. This size sensitivity arises from the code's assumption that size effects can be ignored when the horizontal reinforcement ratio (ρ_h) exceeds a minimum threshold. However, simulation results contradict this assumption, showing shear strength reductions even at ρ_h = 0.80%. This discrepancy highlights the need for code revisions, including: (1) incorporating a scale-dependent concrete contribution correction factor; (2) adjusting strain compatibility for large-scale FRP-concrete interactions; and (3) implementing high thickness ratio-dependent reduction factors. Parametric studies confirm that, while existing codes provide reasonable predictions for standard-sized members, they fail to account for nonlinear size effects in modern large CFRP-reinforced walls, which pose serious safety concerns. Therefore, it is necessary to improve the design provisions by considering size-dependent performance changes in CFRP-reinforced shear walls, which will be addressed in our subsequent work.

Despite the identified code limitations, CFRP-reinforced shear walls demonstrate compelling practical advantages. Field implementations confirm their rapid deploy ability for structural retrofits and superior durability in corrosive environments, yielding lifecycle cost savings [30]. However, achieving the desired performance requires addressing several key implementation challenges. Specifically, ensuring high-quality CFRP-concrete interfacial bonding is critical and may necessitate enhanced surface preparation, automated monitoring of adhesive curing, and rigorous quality control protocols. Additionally, due to CFRP's vulnerability to environmental factors such as UV degradation and fire exposure [81], the use of protective coatings or embedded sensors is essential for maintaining long-term performance. Finally, a comprehensive economic analysis is needed to balance CFRP's lightweight advantages against its higher initial costs [29], particularly in regions where traditional steel reinforcement is prevalent. Future design provisions should integrate these practical considerations to fully unlock CFRP's potential and bridge the gap between theoretical models and real-world applications.

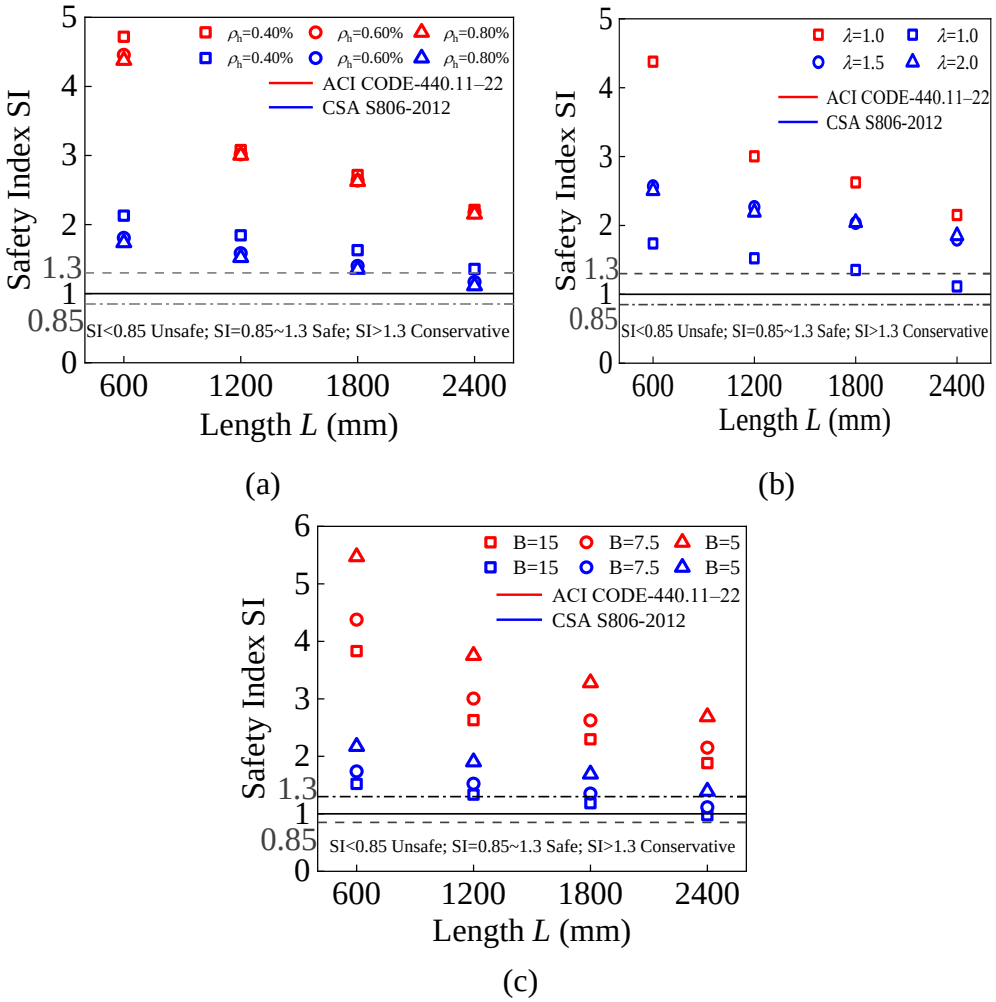

Figure 23. Safety index of several codes: **(a)** horizontal reinforcement ratio; **(b)** shear span ratio; **(c)** height-thickness ratio.

5. Conclusions

This study systematically investigates the seismic performance of CFRP-strengthened shear walls through the numerical simulation of 28 specimens, examining four critical parameters: structural dimensions, shear span ratio, horizontal reinforcement ratio, and height-to-thickness ratio. The parametric analysis identified the main conclusions for shear wall structures under cyclic loading:

Enhanced horizontal reinforcement ratios (ρ_h) demonstrate dual benefits - specimens with ρ_h = 0.80% achieve 5.42% greater shear capacity than ρ_h = 0.40% counterparts while maintaining superior deformation characteristics through improved crack distribution and delayed FRP debonding.

(1) Shear span ratio (λ) significantly influences failure mechanisms, with λ = 2 configurations showing 19.41% reduced shear capacity compared to λ = 1 specimens due to transition from shear-dominated to flexure-shear composite failure patterns. Similarly, height-to-thickness ratio (B) exhibits comparable influence, where slender walls experience 32.25% faster strength degradation than compact sections.

(2) Geometric scaling introduces nonlinear performance deterioration-2400 mm walls demonstrate 25.76% lower nominal shear strength than 600 mm prototypes. The size effect demonstrates sensitivity to key parameters. Shear performance can be optimized by increasing both the shear

span ratio and reinforcement ratio. However, as the height-to-thickness ratio increases, the size effect is further exacerbated.

(3) While increased wall dimensions enhance absolute shear capacity, this scaling concurrently reduces deformation capacity and energy dissipation efficiency, revealing critical trade-offs in seismic design optimization.

While this framework provides theoretical foundations for FRP system optimization, two critical methodological limitations persist. First, the constitutive modeling neglects the inherent material nonlinearity of composite-concrete interfaces under cyclic loading, potentially compromising damage accumulation predictions. Second, the model-experiment validation remains constrained to idealized scenarios. To transcend these constraints, subsequent investigations should prioritize three synergistic advancements: (a) integrating coupled hygro-thermo-mechanical degradation models to address environmental durability gaps under multiaxial seismic excitation, (b) validating against rare earthquake spectra and spatially varying ground motions, and (c) establishing probabilistic links between accelerated laboratory testing and field performance metrics. Such multiscale validation protocols would significantly enhance the framework's capacity to predict infrastructure resilience, particularly for CFRP-reinforced systems operating beyond design-basis earthquake scenarios.

Acknowledgments

This research work was financially supported by the National Natural Science Foundation of China (No. 52208453), and the Natural Science Foundation of Chongqing, China (CSTB2023NSCQ-MSX0682), and the Beijing Nova Program (20220484047). All support is gratefully acknowledged.

Authors' contribution

Bo Li: Methodology, Software, Validation, Formal Analysis, Investigation, Writing—Original Draft Preparation. Dong Li: Supervision, Funding Acquisition, Project Administration. Fengjuan Chen: Project Administration, Writing—Review & Editing, Funding Acquisition, Resources. Liu Jin: Project Administration, Resources, Methodology. Xiuli Du: Project Administration, Resources, Methodology. All authors have read and agreed to the published version of the manuscript.

Conflicts of interests

The authors declare that they have no conflicts of interest, including financial interests, personal relationships, or any other affiliations (such as employment, consulting fees, research contracts, stock ownership, patent licenses, honoraria, or advisory roles) that could have influenced the work reported in this paper.

References

[1] Peng Y, Wu H, Zhuge Y. Strength and drift capacity of squat recycled concrete shear walls under cyclic loading. *Eng. Struct.* 2015, 100:356–368.

[2] Mohamed N, Farghaly A, Benmokrane B, Neale KW. Flexure and shear deformation of GFRP-reinforced shear walls. *J. Compos. Constr.* 2014, 18(2):04013044.

[3] Mohamed N, Farghaly AS, Benmokrane B, Neale K. Evaluation of GFRP-reinforced shear walls. *Canadian society for civil engineering 2013 general conference*, Montréal, Québec, Canada, May 29–June 1, 2013, pp. 1–10.
[4] Massone LM, Orakcal K, Wallace JW. Modeling of squat structural walls controlled by shear. *ACI Struct. J.* 2009, 106(5):646–655.
[5] Mahidul I, Easin A, Azam MSM. Building design for lateral earthquake forces on a multi-story Reinforced Cement Concrete (RCC) structure including a shear wall. *J. ICT des. eng. technol. sci*. 2023, 7(2):7–21.
[6] Ye L, Lu X, Qu Z, Peng F. Analysis on building seismic damage in the Wenchuan earthquake. In *The 14th World Conference on Earthquake Engineering*, Beijing, China, October 12–17, 2008.
[7] Zhao J, Zhao Q, Dang J, Zeng L. Experimental study of deformation behavior of shear wall reinforced with CFRP bars and steel bars. (in Chinese). *Ind. Constr.* 2017, 47(1):163–167.
[8] Li M, Shen D, Yang Q, Cao X, Huang C, *et al*. Effect of reinforcement corrosion on the seismic performance of reinforced concrete shear walls. *Constr. Build. Mater.* 2023, 377:130977.
[9] Sun YP, Takeuchi T, Funato Y, Fujinaga T. Earthquake-resisting properties and evaluation of high-performance concrete columns with low residual deformation. *In Proceedings of the fifteenth world conference on earthquake engineering*, Lisbon, Portugal, September 2012.
[10] Yang J, Li L, Wang X, Hu S. Experimental study on the seismic performance of concrete shear walls partially replaced by MRPC. *Case Stud. Constr. Mater.* 2024, 20:e02695.
[11] Sharma S, Aaleti S, Okumus P. Experimental testing of RC shear wall seismic retrofit using selective weakening, self-centering, and ultra high-performance concrete. *Resilient Cities Struct.* 2023, 2(1):76–90.
[12] Zhang Y, Zhao Q, Zhao K, Hao J, Hu Y. Experimental study on seismic performance of shear wall with insufficient concrete strength strengthened by partial concrete replacement. *Structures.* 2024, 69:107537.
[13] Cardenas AE, Hanson JM, Corley WG, Hognestad E. Design provisions for shear walls. *ACI J.* 1973, 70(3):221–230.
[14] Fintel M. Performance of buildings with shear walls in earthquakes of the last thirty years. *PCI journal.* 1995, 40(3):62–80.
[15] Zheng Y, Zheng S, Yang L, Dong L, Ruan S, *et al*. Experimental study on the seismic behavior of corroded reinforced concrete walls in an artificial climate corrosion environment. *Eng. Struct.* 2022, 252:113469.
[16] Zheng Y, Kang X, Zheng S, Zhang Y, Liu X. Study on seismic behavior of corroded reinforced concrete walls in flexural-shear failure. *Structures.* 2024, 67:107003.
[17] Zhou Y, Zheng S, Chen L, Long L, Dong L, *et al.* Experimental and analytical investigations into the seismic behavior and resistance of corroded reinforced concrete walls. *Eng. Struct.* 2021, 238:112154.
[18] Chen C, Cheng L. Fatigue behavior and prediction of NSM CFRP-strengthened reinforced concrete beams. *J Compos Constr*. 2016, 20(5):04016033.
[19] Chen C, Cheng L. Single crack–based model for FRP shear-strengthened RC beams. *J Compos Constr.* 2019, 23(4):04019030.
[20] Gonzalez-Libreros JH, Sneed LH, D'Antino T, Pellegrino C. Behavior of RC beams strengthened in shear with FRP and FRCM composites. *Eng. Struct.* 2017, 150:830–842.

[21] Zhou H, Attard TL. Rehabilitation and strength sustainability of fatigue damaged concrete–encased steel flexural members using a newly developed polymeric carbon–fiber composite. *Compos. Part B Eng.* 2013, 45(1):1091–103.

[22] Zhou H, Attard TL, Dhiradhamvit K, Wang Y, Erdman D. Crashworthiness characteristics of a carbon fiber reinforced dual-phase epoxy–polyurea hybrid matrix composite. *Compos. Part B Eng.* 2015, 71:17–27.

[23] Yang X, Bai Y, Luo F, Zhao X, Ding F. Dynamic and fatigue performances of a large-scale space frame assembled using pultruded GFRP composites. *Compos. Struct.* 2016, 138:227–236.

[24] Bakis C, Bank L, Brown V, Cosenza E, Davalos JF, *et al*. Fiber-reinforced polymer composites for construction—State-of-the-art review. *J. Compos. Constr.* 2002, 6(2):73–87.

[25] Yang X, Bai Y, Ding F. Structural performance of a large-scale space frame assembled using pultruded GFRP composites. *Compos. Struct.* 2015, 133:986–996.

[26] Ghazizadeh S, Cruz-Noguez CA. Damage-resistant reinforced concrete low-rise walls with hybrid GFRP-steel reinforcement and steel fibers. *J. Compos. Constr.* 2018, 22(2):04018002.

[27] Mohamed N, Farghaly AS, Benmokrane B, Neale KW. Experimental investigation of concrete shear walls reinforced with glass fiber–reinforced bars under lateral cyclic loading. *J. Compos. Constr.* 2014, 18(3):A4014001.

[28] Zhao Q, Zhao J, Dang J, Chen J, Shen F. Experimental investigation of shear walls using carbon fiber reinforced polymer bars under cyclic lateral loading. *Eng. Struct.* 2019, 191:82–91.

[29] Grace NF, Jensen EA, Eamon CD, Shi X. Life-cycle cost analysis of carbon fiber-reinforced polymer reinforced concrete bridges. *ACI Struct. J.* 2012, 109(5):697–704.

[30] Alkhrdaji T, Fyfe ER, Korff J, Schupack M, Bakis CE, *et al*. Guide for the design and construction of structural concrete reinforced with FRP bars. 2006. Available online: https://templet-rebar.com/assets/materials/eng/440.1r-06-guide-for-the-design-and-construction-of-structural-concrete-reinforced-with-frp-bars.pdf (accessed on 27 March 2025).

[31] Kim SW, Jeong CY, Lee JS, Kim KH. Size effect in shear failure of reinforced concrete beams with recycled aggregate. *J. Asian Archit. Build. Eng.* 2013, 12(2):323–330.

[32]Sherwood EG, Bentz EC, Collins MP. Effect of aggregate size on beam-shear strength of thick slabs. *ACI Struct. J.* 2007, 104(2):180.

[33] Li Z, Yu C, Xie Y, Ma H, Tang Z. Size effect on seismic performance of high-strength reinforced concrete columns subjected to monotonic and cyclic loading. *Eng. Struct.* 2019, 183:206—219.

[34] Rasoolinejad M, Bažant ZP. Size effect of squat shear walls extrapolated by microplane model M7. *ACI Struct. J.* 2019, 116(3):75–84.

[35] Song W, Dyke S, Harmon T. Application of nonlinear model updating for a reinforced concrete shear wall. *J. Eng. Mech.* 2013, 139(5):635–649.

[36] Li J, Wang Y, Lu Z, Li J. Experimental study and numerical simulation of a laminated reinforced concrete shear wall with a vertical seam. *Appl. Sci.* 2017, 7(6):629.

[37] Wang M, Wu X. Experimental and numerical investigation on seismic behavior of an innovative superimposed concrete shear wall. *Struct.* 2021, 33:4286–4298.

[38] Jiang Q, Shen J, Chong X, Chen M, Wang H, *et al*. Experimental and numerical studies on the seismic performance of superimposed reinforced concrete shear walls with insulation. *Eng. Struct.* 2021, 240:112372.

[39] Chen J. Experimental study on seismic performance of CFRP-reinforced concrete shear wall. (in Chinese). Zhengzhou:Zhengzhou University, 2015.
[40] Jin L, Miao L, Du X. Influence of shear depth on seismic performance of shear wall reinforced with BFRP bars: mesoscale modeling. *Arch. Civ. Mech. Eng.* 2022, 23(1):4.
[41] Jin L, Zhang B, Chen F, Yu W, Lei Y, *et al*. Numerical investigations on the strain-rate-dependent mechanical behavior and size effect of RC shear walls. *Int. J. Impact Eng.* 2022, 167:104279.
[42] Van Mier JGM, Van Vliet MRA. Influence of microstructure of concrete on size/scale effects in tensile fracture. *Eng. Fract. Mech.* 2003, 70(16):2281–2306.
[43] Chen C, Zhang Q, Keer L, Yao Y, Huang Y. The multi-factor effect of tensile strength of concrete in numerical simulation based on the Monte Carlo random aggregate distribution. *Constr. Build. Mater.* 2018, 165:585–595.
[44] Xia Y, Wu W, Yang Y, Fu X. Mesoscopic study of concrete with random aggregate model using phase field method. *Constr. Build. Mater.* 2021, 310:125199.
[45] Hosseinzadeh M, Dehestani. Three-dimensional multiscale simulations of recycled aggregate concrete employing energy homogenization and finite element approaches. *Constr. Build. Mater.* 2022, 328:127110.
[46] Lin J, Zhao Q, Chen H, Li M, Yuan L. A numerical framework for the ITZ percolation, effective fraction and diffusivity of concrete systems considering the nonuniform ITZ. *J. Build. Eng.* 2023, 77:107429.
[47] Mazzucco G, Pomaro B, Salomoni VA, Majorana CE. Numerical modelling of ellipsoidal inclusions. *Constr. Build. Mater.* 2018, 167:317–324.
[48] Mostofinejad D, Reisi M. A new DEM-based method to predict packing density of coarse aggregates considering their grading and shapes. *Constr. Build. Mater.* 2012, 35:414–420.
[49] Rodrigues ER, Manzoli OL, Bitencourt JAG. 3D concurrent multiscale model for crack propagation in concrete. *Comput. Methods Appl. Mech. Eng.* 2020, 361:112813.
[50] GB 50010-2010. *Code for design of concrete structures*. 1st ed. (In Chinese). Beijing:China Architecture & Building Press, 2010.
[51] Sun G, Gu Q, He R, Fang Y. The energy consumption capacity of steel plate shear wall structure. (In Chinese). *J. Comput. Power Sci.* 2013, 30(3):422-428.
[52] Zhao J, Shen F, Si C, Sun Y, Yin L. Experimental investigation on seismic resistance of RC shear walls with CFRP bars in boundary elements. *Int. J. Concr. Struct. Mater.* 2020, 14:1–20.
[53] Zheng Y, Zhang Y, Zhuo J, Zhang P, Hu S. Mesoscale synergistic effect mechanism of aggregate grading and specimen size on compressive strength of concrete with large aggregate size. *Constr. Build. Mater.* 2023, 367:130346.
[54] Zhou G, Xu Z. 3D mesoscale investigation on the compressive fracture of concrete with different aggregate shapes and interface transition zones. *Constr. Build. Mater.* 2023, 393:132111.
[55] Grassl P, Jirásek M. Meso-scale approach to modelling the fracture process zone of concrete subjected to uniaxial tension. *Int. J. Solids Struct.* 2010, 47(7–8):957-968.
[56] Guan Q, Xu Y, Wang J, Wu Q, Zhang P. Meso-scale fracture modelling and fracture properties of rubber concrete considering initial defects. *Theor. Appl. Fract. Mech.* 2023, 125:103834.
[57] Jumaa GB, Yousif AR. Numerical modeling of size effect in shear strength of FRP-reinforced concrete beams. *Structures.* 2019, 20:237–254.

[58] Huang Y, Yang Z, Chen X, Liu. Monte Carlo simulations of meso-scale dynamic compressive behavior of concrete based on X-ray computed tomography images. *Int. J. Impact Eng.* 2016, 97:102–115.
[59] Chen F, Li B, Li D, Jin L, Du X. Bond stress-slip relationship of CFRP bar-concrete interface of CFRP reinforced concrete subjected to reversed cyclic loading. *Eng. Struct.* 2024, 314:118231.
[60] Chi Y, Yu M, Huang L, Xu L. Finite element modeling of steel-polypropylene hybrid fiber reinforced concrete using modified concrete damaged plasticity. *Eng. Struct.* 2017, 148:23–35.
[61] Wang J, Jivkov A, Li Q, Engelberg D. Experimental and numerical investigation of mortar and ITZ parameters in meso-scale models of concrete. *Theor. Appl. Fract. Mech.* 2020, 109:102722.
[62] Fib-federation internationale du beton (Ed.). F*ib Model Code for Concrete Structures 2010*. Berlin:Ernst & Sohn, 2010.
[63] Guan Q, Xu Y, Wang J, Wu Q, Zhang P. Meso-scale fracture modelling and fracture properties of rubber concrete considering initial defects. *Theor. Appl. Fract. Mech.* 2023, 125:103834.
[64] Yuan W, Wang H, Zhang W, Dai B, Liu K, *et al*. Particle finite element method implementation for large deformation analysis using Abaqus. *Acta Geotech.* 2021:1–14.
[65] Liyue M, Liu J, Fengjuan C, DU X. Experiment study on seismic performance and size effect in BFRP-RC squat shear walls with different horizontal reinforcement ratios. *Eng. Struct.* 2023, 295:116888.
[66] Looi D, Su R, Cheng B, Tsang H. Effects of axial load on seismic performance of reinforced concrete walls with short shear span. *Eng. Struct.* 2017, 151:312–326.
[67] Huang Z, Shen J, Lin H, Song X, Yao Y. Shear behavior of concrete shear walls with CFRP grids under lateral cyclic loading. *Eng. Struct.* 2020, 211:110422.
[68] Naderi S, Tu W, Zhang M. Meso-scale modelling of compressive fracture in concrete with irregularly shaped aggregates. *Cement Concr. Res.* 2021, 140:106317.
[69] Priestley MJN, Kowalsky MJ. Aspects of drift and ductility capacity of rectangular cantilever structural walls. *Bull. N. Z. Soc. Earthquake Eng.* 1998, 31(2):73–85.
[70] Yuan Q, Wang Z, Li H, Zhu H, Suo N. Experimental study on seismic performance of new-type fabricated shear wall with mortar connection. *J. Build. Eng.* 2021, 43:103103.
[71] Calderón S, Sandoval C, Araya-Letelier G, Inzunza E, Arnau O. Influence of different design parameters on the seismic performance of partially grouted masonry shear walls. *Eng. Struct.* 2021, 239:112058.
[72] Jin L, Miao L, Han J, Du X, Wei N, *et al*. Size effect tests on shear failure of interior RC beam-to-column joints under monotonic and cyclic loadings. *Eng. Struct.* 2018:591–604.
[73] Safdari A. Modeling Strength Degradation of Reinforced Concrete Structural Walls. Doctoral Thesis, University of California, Los Angeles,2023.
[74] Guo L, Wang Y, Zhang S. Experimental study of rectangular multi-partition steel-concrete composite shear walls. *Thin-Walled Struct.* 2018, 130:577–592.
[75] Aragaw LF, Calvi PM. Comparing the performance of traditional shear-wall and rocking shear-wall structures designed using the direct-displacement based design approach. *Bull. Earthquake Eng.* 2020, 18(4):1345–1369.
[76] Rasoolinejad M, Bažant ZP. Size effect of squat shear walls extrapolated by microplane model M7. *ACI Struct. J.* 2019, 116(3):75–84.
[77] Miao L, Jin L, Li D, Du X, Zhang B. Effect of shear-span ratio and vertical reinforcement ratio on the failure of geometrical-similar RC shear walls. *Eng. Fail. Anal.* 2022, 139:106407.

[78] ACI Committee 440. *Guide for the design and construction of structural concrete reinforced with fiber-reinforced polymer (FRP) bars (ACI 440.1R-15)*. Farmington Hills, Michigan:American Concrete Institute, 2015.

[79] Canadian Standards Association. Design and construction of building components with fibre-reinforced polymers (No. 2). 2002. Available online: https://giacoketcau.com/download/CSA-S806-02_Design-and-Construction-of-Building-Components-with-Fibre-Reinforced-Polymers.pdf (accessed on 27 March 2025).

[80] Deifalla A. Refining the torsion design of fibered concrete beams reinforced with FRP using multi-variable non-linear regression analysis for experimental results. *Eng. Struct.* 2021, 226:111394.

[81] Wang J, Gangarao H, Liang R, Liu W. Durability and prediction models of fiber-reinforced polymer composites under various environmental conditions: A critical review. *J. Reinf. Plast. Compos.* 2016, 35(3):179–211.